Journal of Sound and Vibration (1997) **202**(3), 313–359

ACTIVE CONTROL OF ENVIRONMENTAL NOISE, II: NON-COMPACT ACOUSTIC SOURCES

S. E. Wright and B. Vuksanovic

*University of Huddersfield, School of Engineering, Huddersfield HD*1 3*DH, England*

(*Received* 21 *November* 1995, *and in final form* 10 *September* 1996)

In this paper the acoustic interference across high frequency finite source distributions in unrestricted space is considered, and how to represent it with a finite number of discrete sources. The problem of creating an acoustic shadow from these sources by using a controlled array of discrete cancellers is then considered. Finally, data is given to illustrate the effectiveness of the approach. It is shown that deep shadows are possible even for complex high frequency sources.

1. INTRODUCTION

This paper is the second in a series on Active Control of Environmental Noise. The first paper [1] was concerned with the basic properties of low frequency acoustic shadows generated by an array of controlled compact cancelling sources, where the acoustic wavelength is large compared with the primary source size. In this situation the radiation field is relatively simple; that is, its amplitude and phase across a wave front change little.

This present paper is concerned with the problem of generating acoustic shadows from complex high frequency sources, or from large extended source distributions where the acoustic wavelength is now small compared with the source dimension. In this case, phase and amplitude vary considerably across the resulting wavefront.

The basic effect of these non-compact free field sources is considered. The problem of representing these source distributions with an array of discrete sources is investigated. The concept of non-discreteness or poor discrete representation is considered, where the acoustic wavelength now becomes small compared to the separation distance between discrete sources.

The extent of the near field from these discrete source arrays is also established, where the simplified far field radiation equation breaks down. Finally the optimization and performance of cancelling arrays to produce acoustic shadows from non-compact, discrete representation of finite source distributions is investigated.

2. FREE FIELD CONCEPTS

2.1. FREE FIELD VERSUS CONFINED RADIATION

There is debate regarding the ability to cancel sound by using active noise control at high frequencies. Also, there is confusion regarding the effectiveness of cancelling sound in enclosures compared to unrestricted space.

0022–460X/97/180313 + 47 $25.00/0/sv960768

Within enclosures, the boundaries dominate through restricting the field. Standing waves occur, through multiple reflection paths, resulting in complex resonant fields for acoustic wavelengths smaller than the enclosure dimensions. In this situation the size of the source is not important and the best that can be hoped for, for high modal density, is cancellation within a fractional wavelength of the error detector.

However, in unrestricted space, the situation is quite different. It is not generally appreciated that if the source, cancelling device and error detector are successively aligned, then the quiet zone can now extend out to infinity, no matter what the frequency. In this case, the complexity of the propagation field now depends on the size of the primary source compared with the acoustic wavelength. Generally, because sources are usually smaller than enclosers, complex radiation from free field sources tends to occur at a much higher frequency, and is of a different nature than that within enclosures.

Most of the contemporary literature is concerned with active noise control in enclosures. The following sections are designed to explore free field concepts and to establish the ability of ANC to suppress non-compact sources outdoors.

2.2. SOURCE NON-COMPACTNESS

In free field, then, it is the primary source size that is important. When the source is small compared with the wavelength, the radiation is basically spherical, with constant phase across its wavefront. As the wavelength λ becomes less than the source size D, i.e., $\lambda/D < 1$, phase changes occur in the radiation field, resulting in destructive interference, particularly at large angles θ from the normal to the source surface.

As the frequency continues to rise, a series of alternate decaying maxima and zeroes occur, as described in more detail in section A4 of the Appendix. The interference function χ_c that describes this effect for a line source, is shown in Figure A3, and is given by equation (A15) as

$$\chi_c = (\sin \gamma)/\gamma, \qquad \gamma = (\pi D \sin \theta)/\lambda. \tag{1}$$

For small γ (low frequencies or small sources) χ_c is unity and no acoustic interference occurs, resulting in a simple propagating field. For higher frequencies or larger sources the first zero ($z = 1$) occurs when $\gamma = \pi$, giving

$$\theta_{z1} = \sin^{-1}(\lambda/D) \tag{2}$$

When $\lambda/D < 1$, $\theta_{z1} < 90^\circ$ and the first zero (phase reversal) for $z = 1$ appears in the radiation field. This provides a convenient definition of the onset of source non-compactness. For multi-dimensional sources, there will be an equivalent interference function for each dimension, as explained in section A6 of the Appendix.

2.3. DISCRETE REPRESENTATION

If the continuous source distribution is now represented by an array of equispaced discrete sources, then the interference function derived in section A8 and shown in Figure A6 becomes, according to equations (A37) and (A38),

$$\chi_d = \sin N\gamma / \sin \gamma, \qquad \gamma = (\pi d \sin \theta)/\lambda. \tag{3}$$

Here d is the separation distance between sources ($d = D/N - 1$) and N is the number of discrete sources across the distribution. Now the first zero is when $N\gamma = \pi$.

Additionally, this function has non-decaying major maxima occurring when $\gamma = m\pi$, where m is an integer. These major maxima sandwich $N - 2$ minor maxima and must be avoided for good discrete representation of continuous source distributions. The first

major maximum ($m = 1$) occurs when $\gamma = \pi$, giving

$$\theta_{m1} = \sin^{-1}(\lambda/d). \tag{4}$$

When $\lambda/d < 1$, $\theta_{m1} < 90^\circ$ and the first major maximum appears in the radiation field. In this case χ_d ceases to become similar to, or representative of, χ_c, thus providing a convenient definition of the onset of poor discrete representation, or non discreteness, when $\lambda/d < 1$.

2.3. NEAR FIELD

Finally the extent of the near field, where the above far field radiation equations become invalid, is considered in section A3 of the Appendix. Here, because of a range of source–observer distances, it is not possible to obtain closed form solutions and computed fields have to be relied on.

On approaching a source the sound pressure usually doubles (increases 6 dB) per halving of the distance to the source. For a non-compact source this doubling ceases at some distance from the source, through destructive interference across the finite source distribution.

The onset of this near field effect can be approximated by the first zero as the observer approaches the source, given by equation (A11c), as

$$r_{z1} \simeq (D\cos\theta)^2/4\lambda. \tag{5}$$

It can be seen from this equation that the near field is directional, stretching away from the centre of the source and increasing with frequency and source size.

3. COMPUTATIONS

3.1. COMPACTNESS AND DISCRETENESS

The compactness (λ/D) for a continuous source distribution, and the discreteness (λ/d) for an array of discrete sources representing a continuous source distribution are summarized in Table 1. Here λ, D and d are the wavelength, source size and discrete source separation distance respectively. p and N are the total number of discrete sources and the number of sources per row or column for a square source distribution, respectively.

For simplicity, λ is taken as 4 m at 100 Hz (instead of 3·43 m). The range of frequencies 100–6400 Hz and source sizes 0·25–4·0 m covers the parameter sizes of interest. The computation is performed for $D = 2$ m. For laboratory investigations $D = 1$ m is more practical, and for outside full scale measurements $D = 4$ m is more appropriate.

The heavily shaded areas give the onset of non-compactness ($\lambda/D = 1$). For values less than one, the source is regarded as non-compact. The lightly shaded areas give the onset of non-discreteness ($\lambda/d = 1$). For values less than one, the source is considered to have poor discrete representation. For instance, a 2 m square source will cease to be compact at $f = 200$ Hz, and will require a discrete source spacing less than $d = 2$ m for good discrete representation.

3.2. STANDARD CASE

The acoustic field is observed over a $60^\circ \times 60^\circ$ observer sector of a sphere 50 m normal to the centre of a $D = 2$ m square source. The primary source is a simulated continuous source distribution with an excessively large number of discrete sources (40 rows by 40

TABLE 1

The determination of source compactness ($\lambda/D > 1$) and source discreteness ($\lambda/d > 1$) for various source frequencies (f), sizes (D) and numbers of point sources (p)

f (Hz)		100	200	400	800	1600	3200	6400
λ (m) (≈)		4	2	1	1/2	1/4	1/8	1/16
D = 1/4 (0.22 m)	λ/D	16	8	4	2	1	1/2	1/4
	p = 4, N = 2, d = 1/4	16	8	4	2	1	1/2	1/4
	p = 9, N = 3, d = 1/8	32	16	8	4	2	1	1/2
	p = 25, N = 5, d = 1/16	64	32	16	8	4	2	1
D = 1/2 (0.43 m)	λ/D	8	4	2	1	1/2	1/4	1/8
	p = 4, N = 2, d = 1/2	8	4	2	1	1/2	1/4	1/8
	p = 9, N = 3, d = 1/4	16	8	4	2	1	1/2	1/4
	p = 25, N = 5, d = 1/8	32	16	8	4	2	1	1/2
D = 1 (0.86 m)	λ/D	4	2	1	1/2	1/4	1/8	1/16
	p = 4, N = 2, d = 1	4	2	1	1/2	1/4	1/8	1/16
	p = 9, N = 3, d = 1/2	8	4	2	1	1/2	1/4	1/8
	p = 25, N = 5, d = 1/4	16	8	4	2	1	1/2	1/4
D = 2 (1.72 m)	λ/D	2	1	1/2	1/4	1/8	1/16	1/32
	p = 4, N = 2, d = 2	2	1	1/2	1/4	1/8	1/16	1/32
	p = 9, N = 3, d = 1	4	2	1	1/2	1/4	1/8	1/16
	p = 25, N = 5, d = 1/2	8	4	2	1	1/2	1/4	1/8
D = 4 (3.43 m)	λ/D	1	1/2	1/4	1/8	1/16	1/32	1/64
	p = 4, N = 2, d = 4	1	1/2	1/4	1/8	1/16	1/32	1/64
	p = 9, N = 3, d = 2	2	1	1/2	1/4	1/8	1/16	1/32
	p = 25, N = 5, d = 1	4	2	1	1/2	1/4	1/8	1/16

columns of sources: i.e., $N = 40$ and $p = 1600$). The total source strength of all sources is $Q_p = p \times q_p = 1\ \mathrm{m}^3/\mathrm{s}$, and from equation (A46) the separation distance between sources is $d = D/(n - 1) = 2/39 = 0{\cdot}051$ m. The speed of sound is taken as $c = 343$ m/s and the

density of air $\rho = 1{\cdot}21$ kg/m^3. For sound pressure normal to the source surface ($\theta = 0^\circ$) then $\sin\gamma/\gamma = 1$ in equation (A15), and from equation (A3) the sound pressure amplitude is then given by

$$P = (\rho Q/2r_o)f = 0{\cdot}0121f. \tag{6}$$

For example, if $f = 100$ Hz, $P = 1{\cdot}21$ Pascals, or in dB relative to 20 μPa (threshold of hearing)

$$P = 20\log\left(\frac{1{\cdot}21}{20}\,10^6\right) = 95{\cdot}64\text{ dB} \approx 96\text{ dB}. \tag{7}$$

For each doubling in frequency, 6 dB is added.

3.3. MARGINALLY COMPACT SOURCE

For Figure 1(a) the frequency is chosen so that the source is marginally compact; i.e., $\lambda/D = 1$. For a source dimension of 2 m, the wavelength λ must be 2 m, giving a frequency $f = c/\lambda = 343/2 = 171$ Hz. Also for d above, $\lambda/d = 39$, which confirms good discrete representation or a near continuous source description. The spherical-like directivity pattern visible in relief and circular rings in contour shows a modest off-axis sound reduction. This corresponds to the $(\sin\gamma)/\gamma$ interference function becoming less than unity as the observer angle θ increases from 0° to $\pm 30^\circ$, giving $\chi_c = 0{\cdot}64$ or $-3{\cdot}9$ dB. For $\lambda/D \gg 1$ or $\theta_z \gg 90^\circ$ (that is, a compact or near point source situation) the directivity function would become unity, giving a flat directivity (equal sound pressure) over the $60^\circ \times 60^\circ$ observer sector.

3.4. NON-COMPACT SOURCE

In Figure 1(b) is shown the effect of considerable acoustic interference for a non-compact source, again with near continuous source representation ($p = 1600$). Here the frequency has been increased to $f = 800$ Hz, $\lambda = 0{\cdot}429$ m, making $\lambda/D = 0{\cdot}214$ and $\lambda/d = 8{\cdot}36$, confirming the non-compact "continuous" source condition. The resulting complex interference pattern can be understood by referring to Figure A3. Here, there is a zero order maximum of unity, ($\sin\gamma/\gamma = 1$ (0 dB), then a first order maximum of 0·2 (14 dB down) followed by a succession of maximums that decay at 6 dB per doubling in angle. The first zero (θ_{z1}) and maximum (θ_{n1}) predicted by equations (A20) and (A18) are $\theta_{z1} = \sin^{-1}(\lambda/D) = 12{\cdot}4^\circ$ and $\theta_{n1} = \sin^{-1}(3\lambda/2D) = 18{\cdot}8^\circ$, followed by multiple zeros approximately every 12.4°. The slight distortion towards the corners of the directivity, is caused through the atlas effect; i.e., projecting a spherical surface on to a flat plane.

3.5. POOR DISCRETE SOURCE REPRESENTATION

In Figure 1(c) is shown the same non-compact source situation ($D = 2$, $f = 800$ Hz, $\lambda = 0{\cdot}429$ m, $\lambda/D = 0{\cdot}214$), except that here it has poor discrete representation. The source distribution of 1600 point sources is now replaced by only three rows by three columns of sources, giving a total of nine point sources; i.e., $p = 9$, $N = 3$. The acoustic interference pattern is now considerably changed.

To understand the new pattern it is useful to refer now to Figure A6. Here, there is a series of non-decaying (equal amplitude) major maxima, sandwiching ($N_n = N - 2 = 1$) minor maxima. The separation between sources is $d = D/(N-1) = 2/(3-1) = 1$ m, giving $\lambda/d = 0{\cdot}429$. One sees from equation (A45) that the first zero occurs at $\theta_{z1} = \sin^{-1}(\lambda/Nd) = 8{\cdot}2^\circ$. From equation (A43) the first minor maximum occurs at

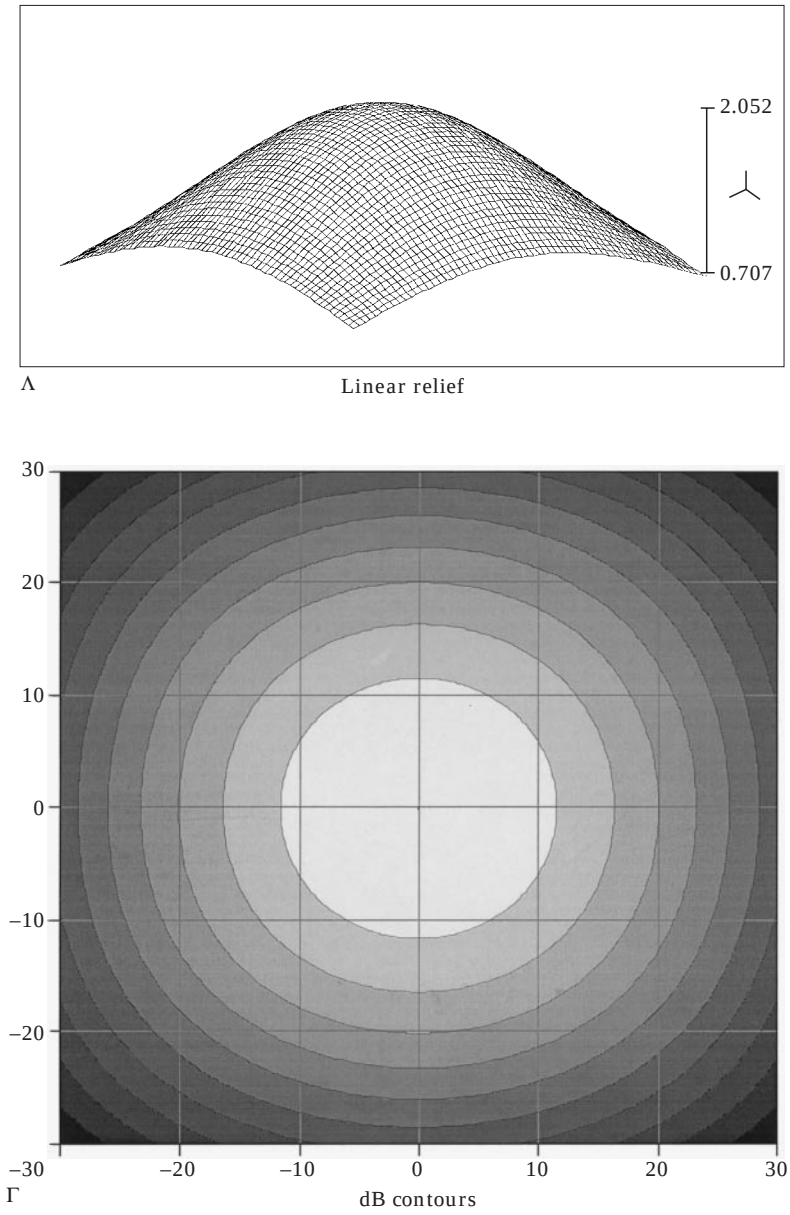

Figure 1(a). Marginally compact source.

$\theta_{n1} = \sin^{-1}(3\lambda/2Nd) = 12{\cdot}4^\circ$, and from equation (A41) the first major maximum occurs at $\theta_{m1} = \sin^{-1}(\lambda/d) = 25{\cdot}4^\circ$. The zero order major maximum ($m = 0$) occurs at 0°. By comparing Figures 1(b) and 1(c) it can be seen that θ_{m1} does not exist for the continuous source case ($\theta_{m1} \gg 90^\circ$) producing decaying radiation with observer angle, whereas the poor discrete representation case has non-decaying major maxima occurring across the observation window. Also there is considerable error for θ_{n1} and θ_{z1} for the poor discrete source representation case ($6{\cdot}4^\circ$ and $4{\cdot}2^\circ$ respectively).

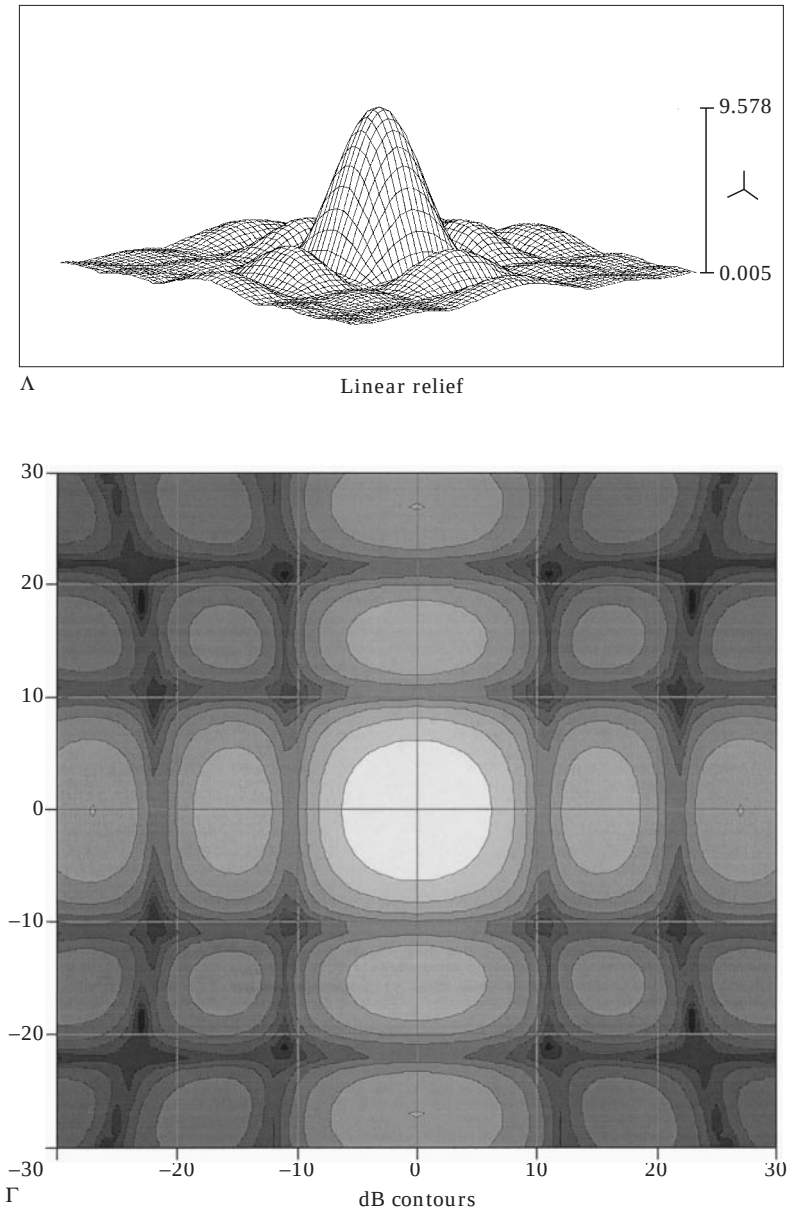

Figure 1(b). Non-compact source.

3.6. MARGINAL DISCRETE SOURCE REPRESENTATION

Figure 1(d) was computed for the same conditions as Figure 1(c) except that the source matrix is now increased to $p = 6 \times 6$, giving $\lambda/d = 1{\cdot}07$. This now gives marginally discrete source representation, where $\theta_{m1} = 90^\circ$, $\theta_{n1} = 15{\cdot}5^\circ$, $\theta_{z1} = 10{\cdot}2^\circ$ and $N_n = N - 2 = 4$ minor maxima between the two major maxima, situated at 0° and 90°. It can be seen now that the directivity looks much more like the continuous source representation of Figure 1(b), although λ/d has been increased only by a factor of two. For many cases this discrete representation ($\lambda/d \approx 1$) is adequate.

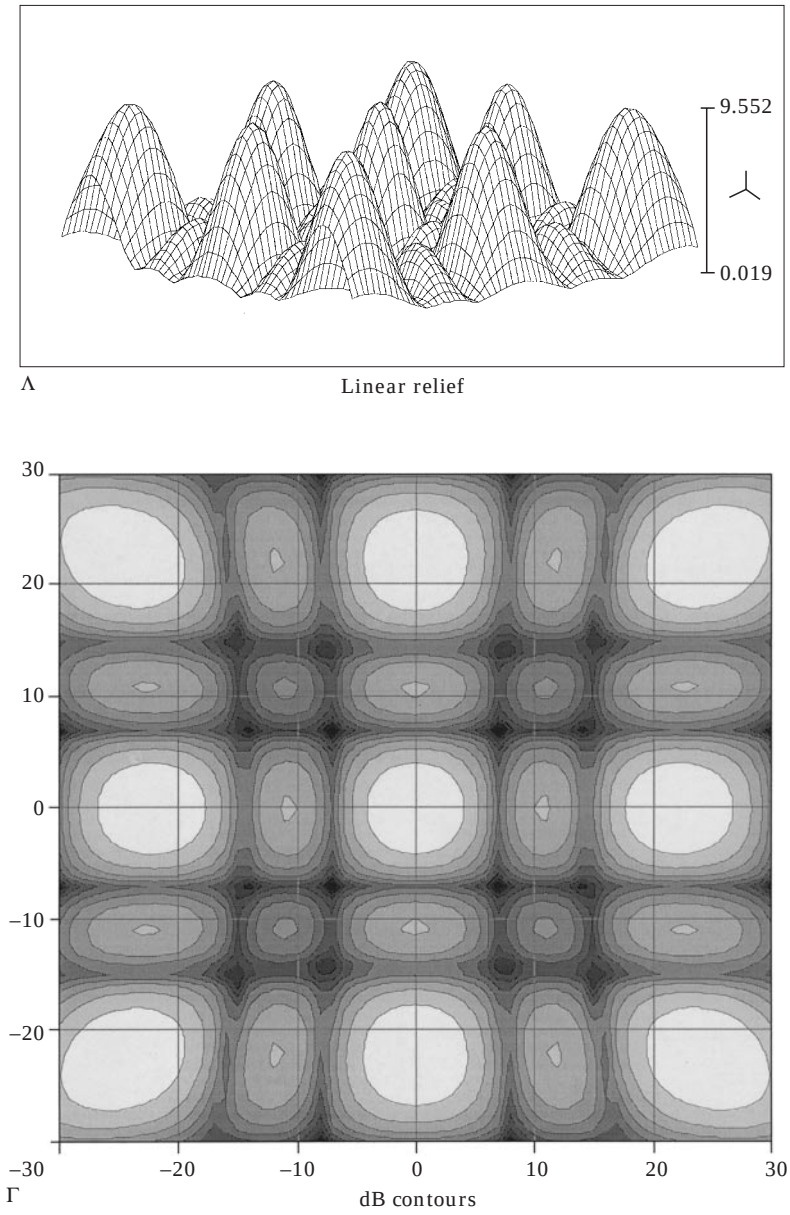

Figure 1(c). Pour discrete source representation.

3.7. NEAR FIELD-DISCRETE SOURCES

In Figure 2(a) is illustrated the effect of the near field for various numbers of primary sources p. The curve labelled $p = 3$ is for a 800 Hz line source of length $D = 2$ m comprising three discrete sources, one in the centre and two at the ends. The onset of the near field for an observer moving perpendicular ($\theta = 0^\circ$) to the line source and through the centre is clearly shown. The first zero on approaching the source, r_{z1} for $p = 3$, is predicted by equation (A11c) as $(D \cos\theta)^2/4\lambda \approx 2{\cdot}3$ m ($5{\cdot}36\lambda$).

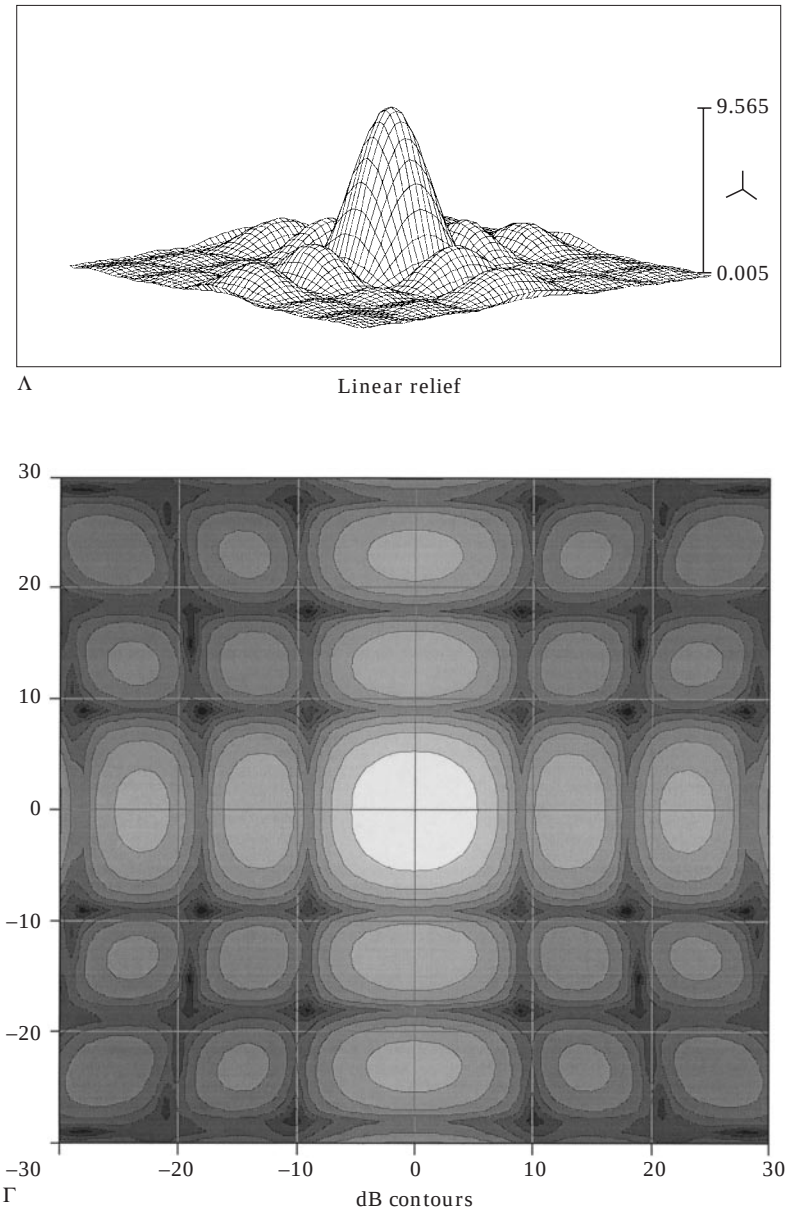

Figure 1(d). Marginal discrete source representation.

Figure 1. The effect of source compactness and discreteness on the directivity pattern ($D = 2$ m, $\theta_o = 60^\circ \times 60^\circ$, $r_o = 50$ m). (a) Marginally compact source ($\lambda/D = 1$) with "continuous" representation ($\lambda/d = 39$, $f = 171$ Hz, $p = 40 \times 40$). (b) Non-compact source ($\lambda/D \approx 0{\cdot}214$) with "continuous" representation ($\lambda/d \approx 8{\cdot}36$, $f = 800$ Hz, $p = 40 \times 40$). (c) Non-compact source ($\lambda/D \approx 0{\cdot}214$) with poor discrete representation ($\lambda/d \approx 0{\cdot}429$, $f = 800$ Hz, $p = 3 \times 3$). (d) Non-compact source ($\lambda/D \approx 0{\cdot}214$) with marginal discrete representation ($\lambda/d \approx 1$, $f = 800$ Hz, $p = 6 \times 6$).

The actual start of the near field can be seen to be at least twice that predicted for the first zero. Also, note that the sound pressure becomes very large as the observer approaches the discrete source at the centre of the source distribution. The two other

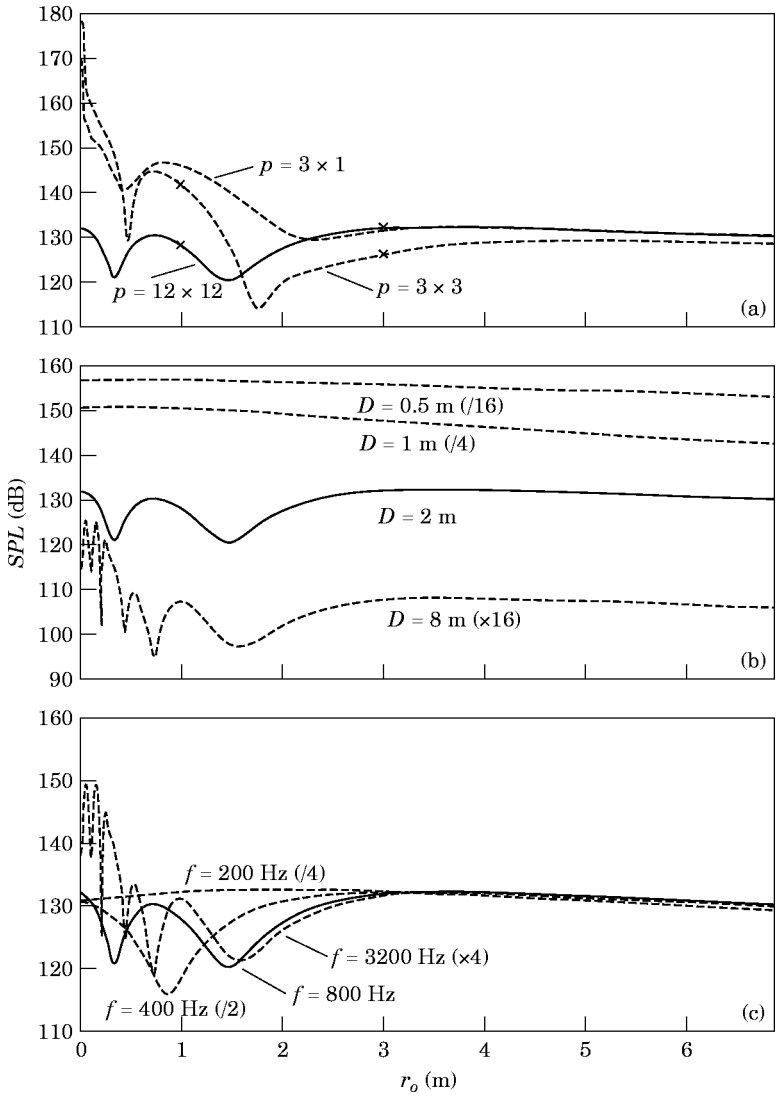

Figure 2. The onset of the near field. (a) Effect of primary source number p ($D = 2$ m, $f = 800$ Hz); (b) effect of source size D ($f = 800$ Hz, $p = 12 \times 12$); (c) effect of frequency f ($D = 2$ m, $p = 12 \times 12$).

computed curves are for a 2 m square source, one comprising three rows by three columns of sources ($\lambda/d \approx 0{\cdot}429$) and the other consisting of 12 by 12 sources ($\lambda/d \approx 2{\cdot}36$). All three curves are similar, except that the position of the first zero moves slightly closer to the source as the number of sources increases. The r_{z1}, for $p = 3$, is therefore the worst case prediction.

3.8. NEAR FIELD: CONTINUOUS SOURCES

In the case of the 12×12 source distribution (no centre source), the sound pressure ceases to increase exponentially as the observer approaches the centre of the distribution. Instead, it attains a finite amplitude similar to that of a continuous source distribution. A fourth condition was also computed by using a matrix of 40×40 sources. This gave almost identical results to the 12×12 source, showing that the 12×12 was already representative of a continuous source distribution.

In Figure 2(b) is shown the effect of source size for the "continuous" source case ($p = 12 \times 12$), again for a source frequency of 800 Hz. Increasing the source size by a factor of four ($D = 2$ m$\rightarrow$8 m, $\lambda/D = 0{\cdot}214\rightarrow0{\cdot}053$) increases the near field first zero r_{z1} by a factor of 16, according to equation (A11c). (The $D = 8$ m horizontal scale has been reduced by a factor of 16.) Decreasing the source size by a factor of four ($D = 2$ m$\rightarrow$0·5 m, $\lambda/D = 0{\cdot}214\rightarrow0{\cdot}856$) approaches the compact source condition with seemingly no near field zeros. The *SPL* in the far field decreases with increasing distance (16 times = 24 dB). The *SPL* in the near field increases as the source becomes more compact.

In Figure 2(c) is shown the effect of frequency on the near field zeros. Increasing the frequency by a factor of four ($f = 800$ Hz$\rightarrow$3200 Hz, $\lambda/D = 0{\cdot}214\rightarrow0{\cdot}053$) increases r_{z1} by a factor of four according to equation (A11c). (Here the $f = 3200$ Hz horizontal scale has been reduced by a factor of four.) Note that the interference structure (near field zeros) is exactly the same as for $D = 8$ m in Figure 2(b), except that the higher frequency zeros are closer to the source. Decreasing the frequency by a factor of four ($f = 800$ Hz$\rightarrow$200 Hz, $\lambda/D = 0{\cdot}214\rightarrow0{\cdot}856$), one again approaches the compact source condition with no near field zeros. The *SPL* in the far field remains approximately the same, as the frequency:distance ratio remains the same. The *SPL* in the near field increases with increasing frequency.

3.9. NEAR FIELD PREDICTION

From the data given in Figure A2 there does not appear to be an appreciable near field for compact sources with $\lambda/D > 0{\cdot}5$. For non-compact "continuous" sources, $\lambda/D < 0{\cdot}5$, the near field first zero r_{z1} is given approximately by

$$r_{z1} = D^2/6\lambda. \tag{8}$$

The effect of the directivity term $\cos\theta$ in equation (A11c) is not clearly apparent. It is masked by the noncompact directivity terms $(\sin\gamma)/\gamma$ in equation (A15) for angles $\theta > 0$.

3.10. NEAR FIELD DIRECTIVITY PATTERNS

In Figures 3(a)–(d) is shown the directivity of an 800 Hz, $60^\circ \times 60^\circ$ observer sector at radius of 3 m (7λ) and 1 m ($2{\cdot}3\lambda$) from the centre of a $p = 12 \times 12$ and $p = 3 \times 3$, 2 m square source surface (positions indicated by a cross on Figure 2(a)). These patterns are now complex, as they are again a combination of both non-compact and near field interference patterns.

In Figure 3(a), for $r_o = 3$ m and $p = 12 \times 12$, considerable change in directivity is shown at the onset of the near field compared with the far field (Figure 1(b)). However, the original pattern away from the centre of the pattern can still be recognized. In Figure 3(b), for $r_o = 1$ m, the pattern has developed into a large *SPL* dominating the central part of the pattern, although the maximum level is still similar to that for the 3 m position, with a minimum in between, as can be seen in Figure 2(a).

In Figure 3(c) is illustrated the near field for a poor discrete source representation case ($p = 3 \times 3$). Here the pattern at 3 m is barely recognizable with respect to the far field case (Figure 1(c)). However, the sound pressure remains high across the whole window, corresponding to the non-decaying major maxima shown in Figure 1(c). As the observer approaches the source even more closely ($r_o = 1$ m), as in Figure 3(d) the window is again dominated by a large central *SPL*. This can be confirmed in Figure 2(a), where the level is now considerably higher for the closer source position, again with a minimum in between the two positions.

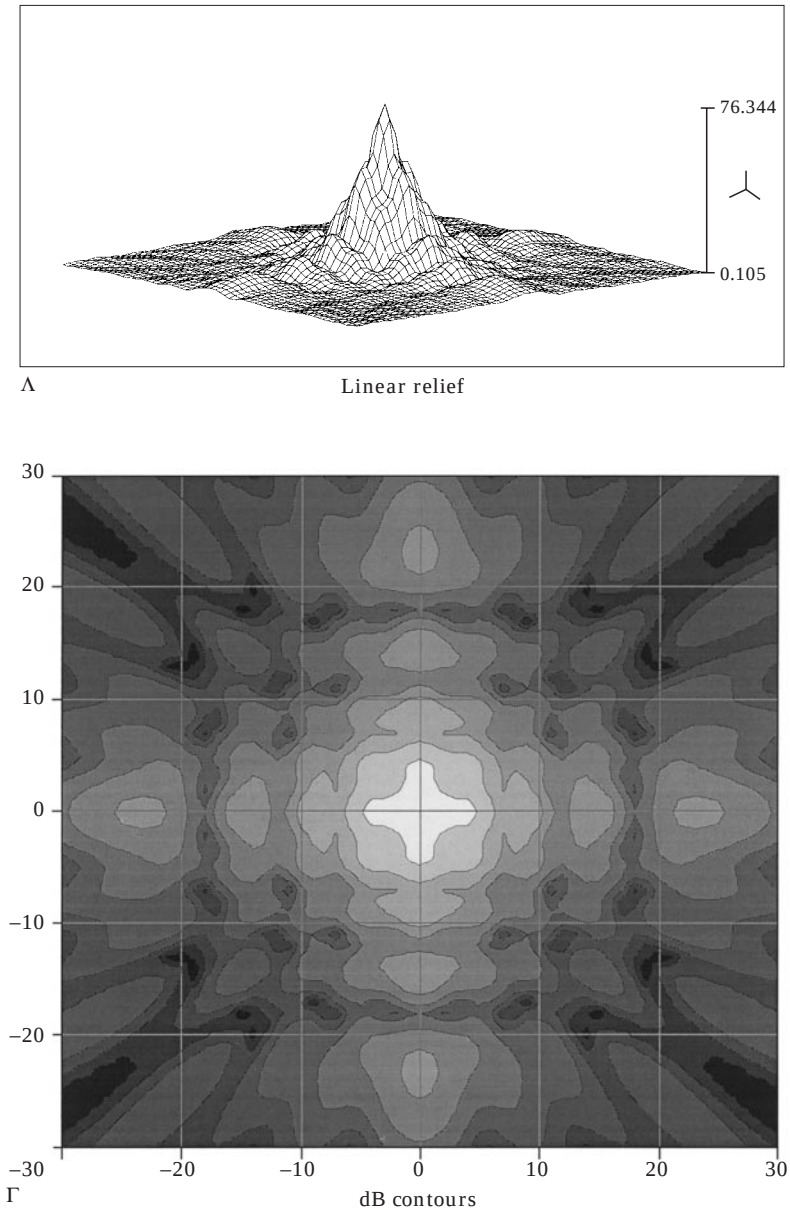

Figure 3(a). $p = 12 \times 12$, $r_0 = 3$ m.

3.11. NEAR FIELD GENERALLY

According to equations (5) and (8), low frequency compact sources ($\lambda/D \gg 1$) have small simple (monophase) near fields. For high frequency non-compact sources ($\lambda/D \ll 1$) the near field extends to considerable distances in front of the source, and its field is complex (multi-phased).

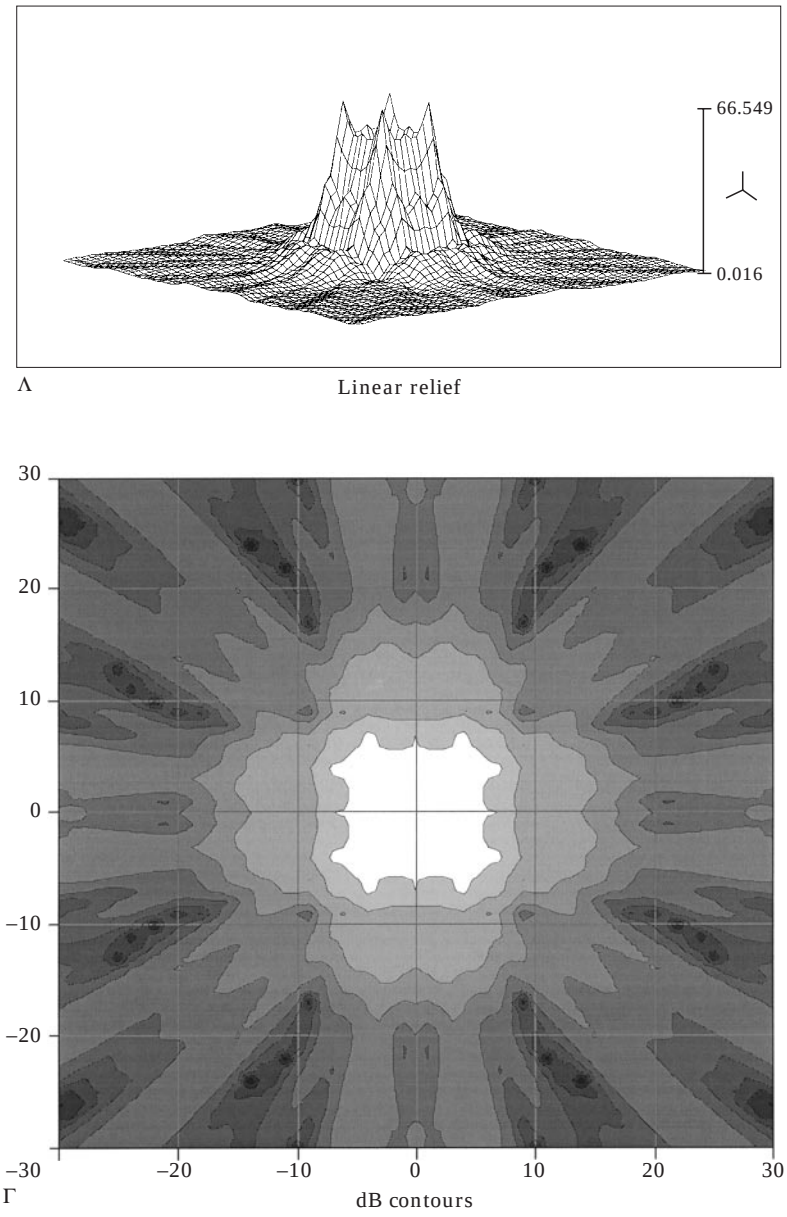

Figure 3(b). $p = 12 \times 12$, $r_0 = 1$ m.

3.12. EFFECT OF FREQUENCY ON DIRECTIVITY PATTERN

In Figures 4(a)–(d) is shown the effect of varying the primary source frequency on the far field source directivity pattern. The source is 2 m square, radiating at 200, 400, 800 and 1600 Hz, giving compactness factors of $\lambda/D = 0{\cdot}86$, $0{\cdot}43$, $0{\cdot}215$ and $0{\cdot}107$, respectively. The source has near continuous source representation (i.e., $p = 1600$, $N = 40$) and the radiation pattern is measured over a 60° window at an observer distance of 50 m.

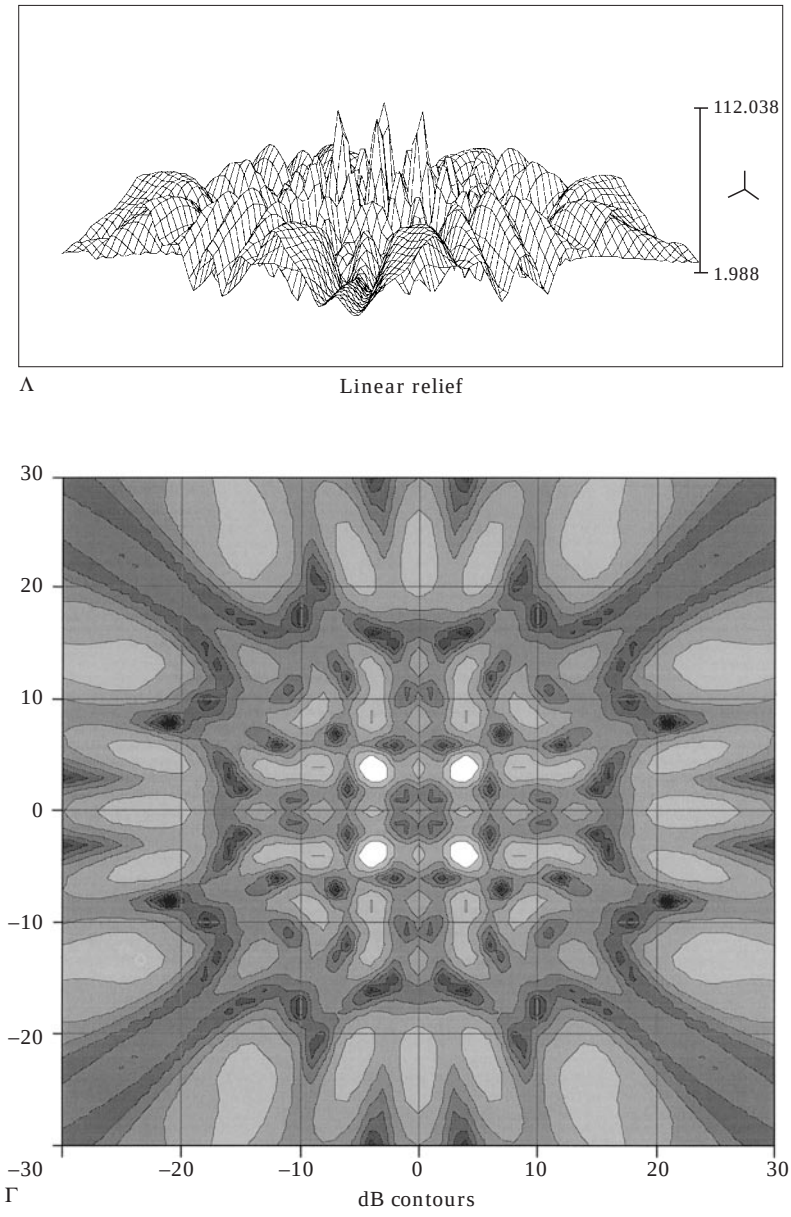

Figure 3(c). $p = 3 \times 3$, $r_0 = 3$ m.

The relief figures show the actual levels in linear scale; the contour plots are in dB, exaggerating the lower levels, more like an audibility response. The figures show increasing acoustic beaming normal to the surface and linearly increasing sound pressure according to equations (6) and (7) as the frequency increases: 2·42 Pa (102 dB), 4·84 Pa (108 dB), 9·68 Pa (114 dB) and 19·36 Pa (120 dB). The first zero for each of the increasing frequencies is at 59·3°, 25·5°, 12·4° and 6·1° respectively; the zero at 59·3° is of course outside the $\pm 30^\circ$ window.

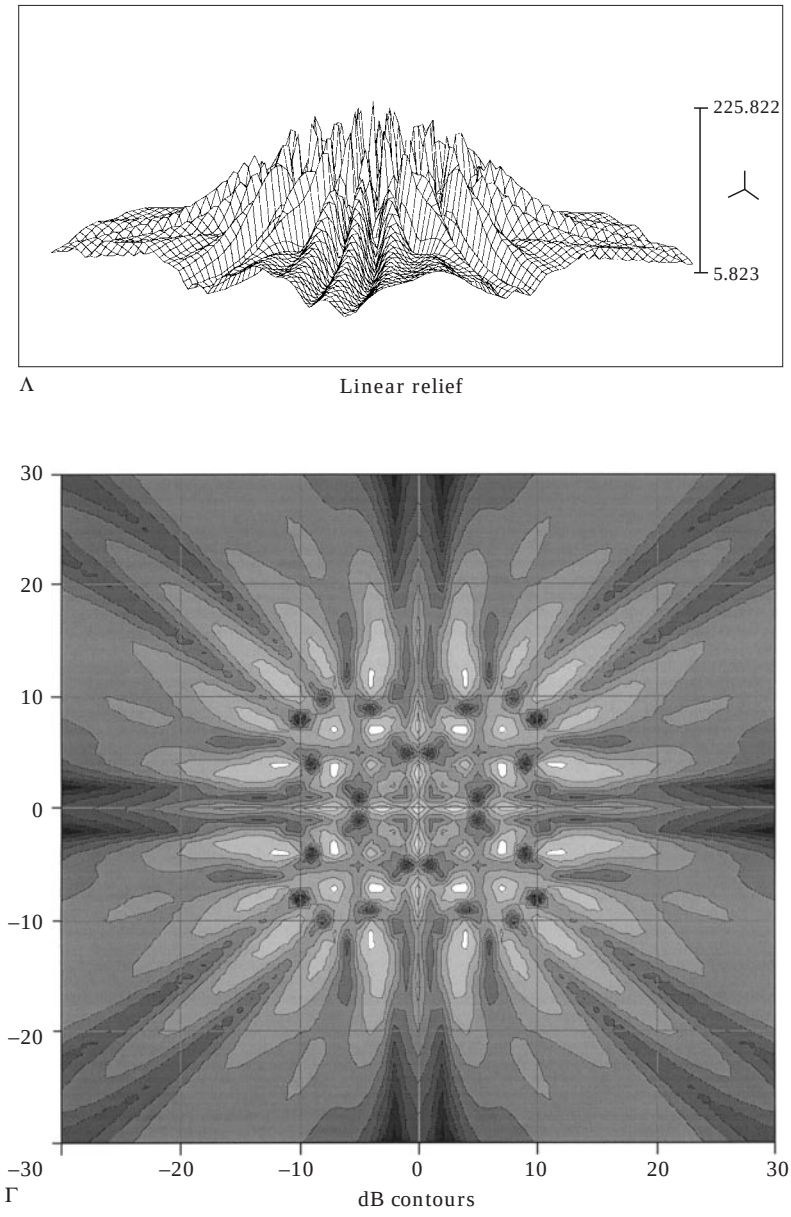

Figure 3(d). $p = 3 \times 3$, $r_0 = 1$ m.

Figure 3. The effect of the near field on the directivity pattern for various observer distances (r_o) and source numbers (p) ($D = 2$ m, $f = 800$ Hz, $\theta_o = 60^\circ \times 60^\circ$). (a) Near field, $p = 12 \times 12$, $r_o = 3$ m; (b) near field, $p = 12 \times 12$, $r_o = 1$ m; (c) near field, $p = 3 \times 3$, $r_o = 3$ m; (d) near field, $p = 3 \times 3$, $r_o = 1$ m.

3.13. 360° AZIMUTHAL DIRECTIVITIES

Although it is useful to investigate the radiation in detail over a $60^\circ \times 60^\circ$ window in front of the source, it is also important to know what is happening across the full 360°: i.e., all around the source. To do this economically, and on a flat piece of paper,

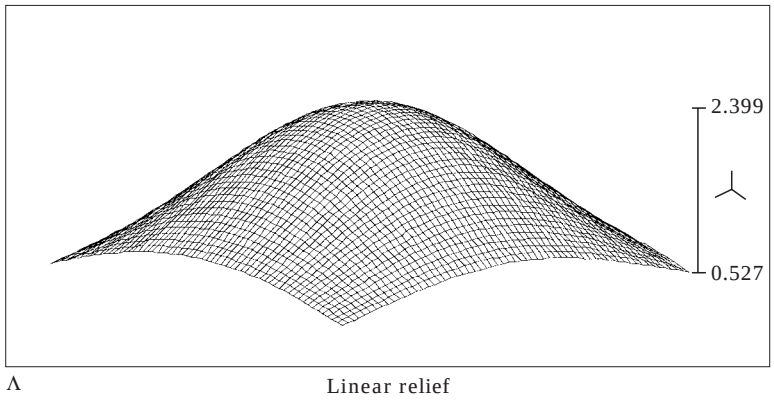

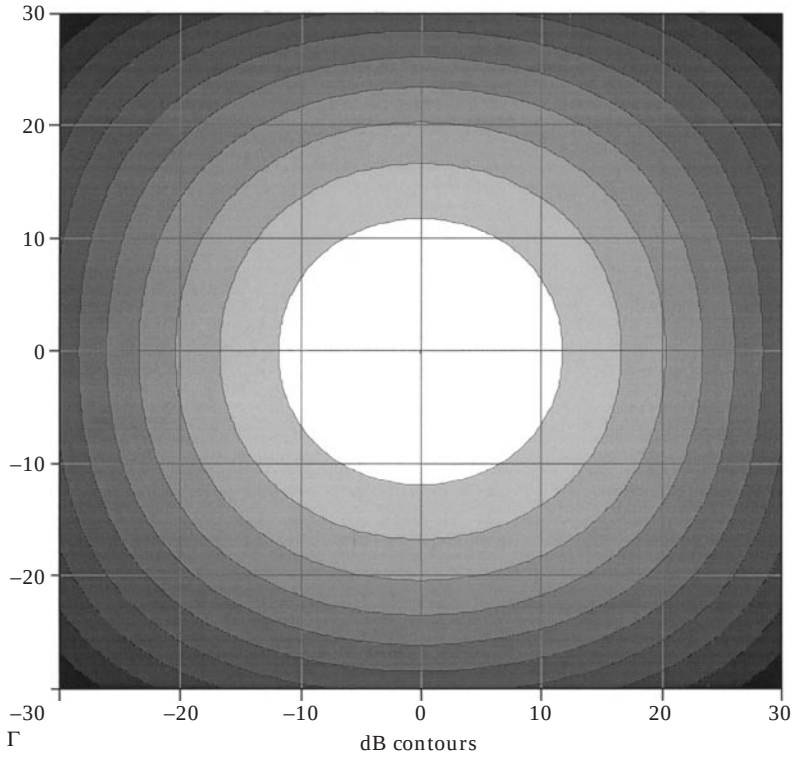

Figure 4(a). $f = 200$ Hz.

a $360^\circ \times 60^\circ$ observer strip is used, as shown in Figures 5(a)–(d). Again slight distortion is observed towards a $\pm 30^\circ$ elevation angle, due to the atlas effect. Three directivity patterns, dB relief, dB contour and averaged *SPL* over a 15° elevation angle at an observer distance $r_o = 50$ m are shown. These directivities are repeated for four frequencies, 200, 400, 800 and 1600 Hz, for $p = 40 \times 40$ and $D = 2$ m. The maximum sound pressure from equation (7), for example for 800 Hz and $\theta = 0^\circ$, is 114 dB. Doubling and halving the frequency adds and subtracts 6 dB, respectively.

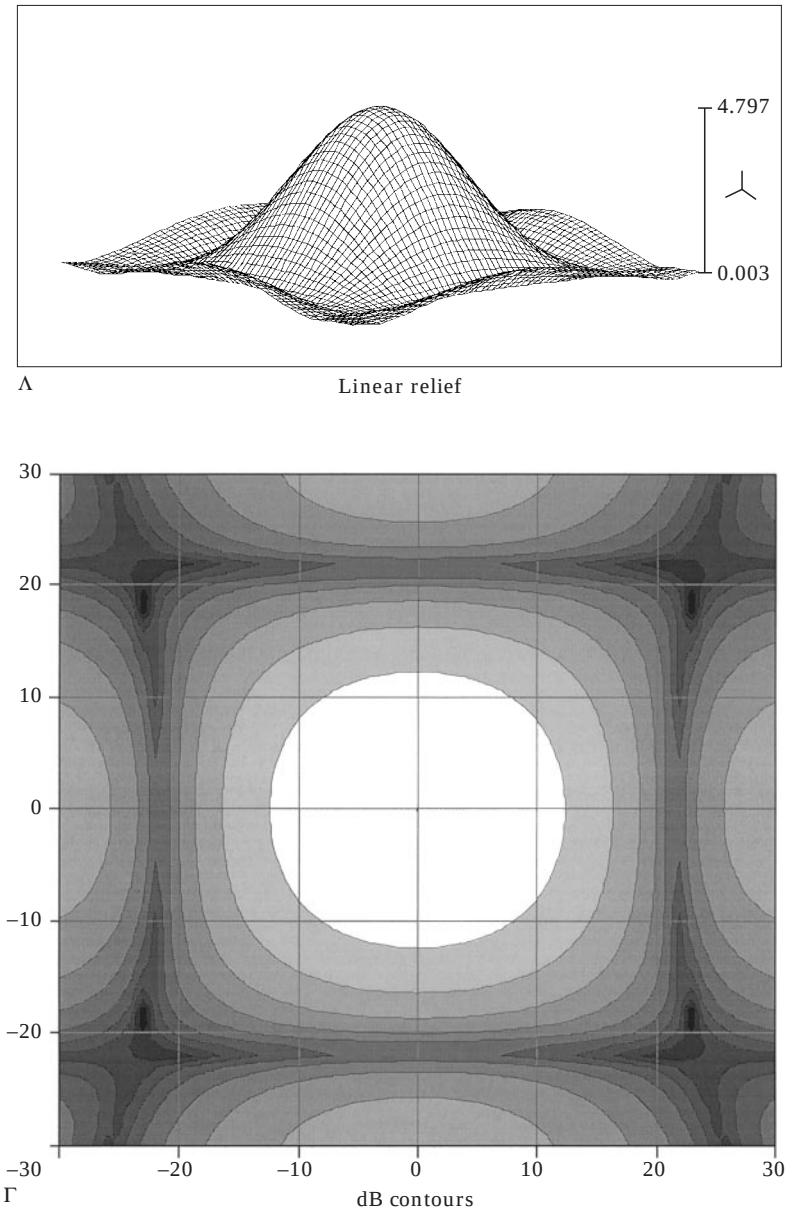

Figure 4(b). $f = 400$ Hz.

4. ACOUSTIC SHADOWS

4.1. GENERATING ACOUSTIC SHADOWS

It can be seen from Figure 1 that, to represent continuous source distributions adequately by a discrete array of primary sources, then $\lambda/d_p > 1$. Likewise, it can be anticipated that to generate an equal but opposite polarity anti-shadow, to form the shadow, a similar number of secondary cancelling sources with the appropriate phase and amplitude will be required; i.e., $\lambda/d_s > 1$. That is, good discrete representation is also

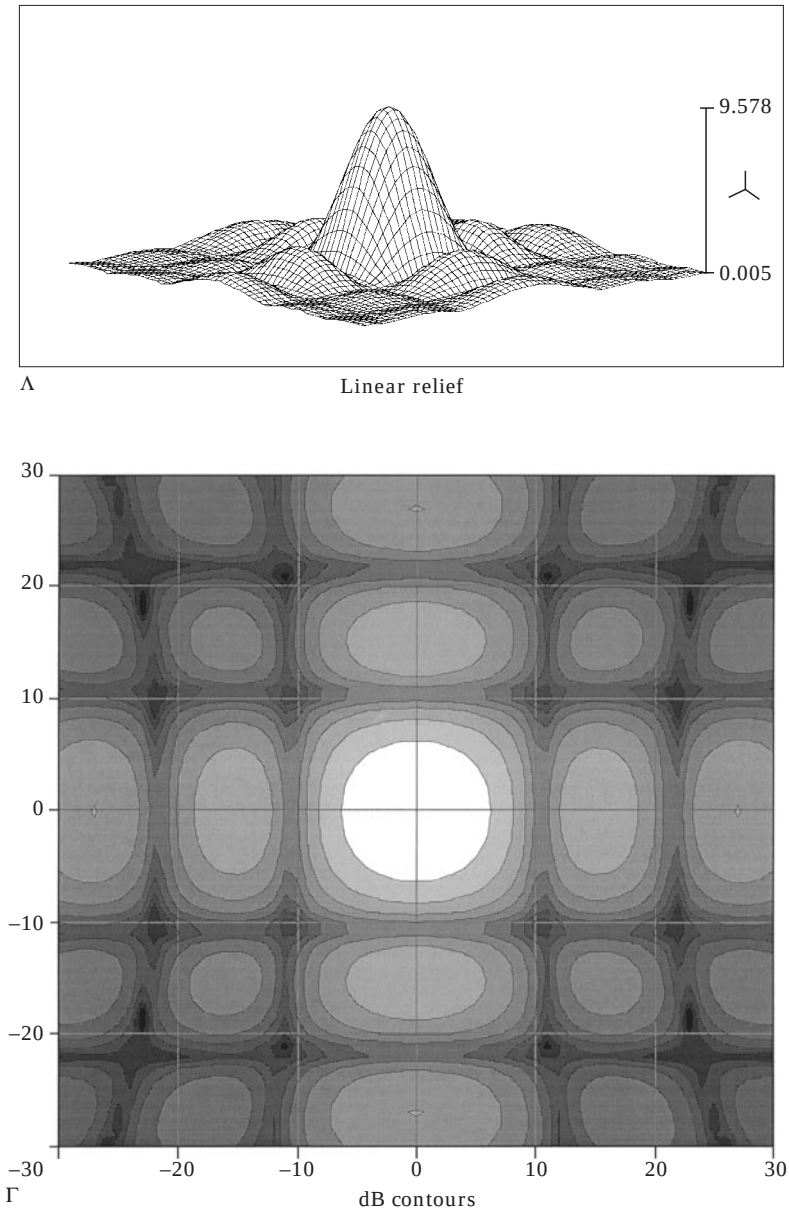

Figure 4(c). $f = 800$ Hz.

needed, for arrays of cancelling sources, to produce deep shadows. Therefore, Table 1 is equally applicable in determining deep shadows, as in establishing good discreteness.

4.2. $15^\circ \times 15^\circ$ STANDARD SHADOW

In Figure 6 are shown the details of a 400 Hz ($\lambda = 0{\cdot}858$ m) shadow from a 2 m square source ($\lambda/D = 0{\cdot}429$). The shadow is generated by a 3×3 array of secondary sources (cancellers) equi-spaced over a $15^\circ \times 15^\circ$ control angle ($d = D/N - 1 = 1$ m, $\lambda/d = 0{\cdot}858$). The cancellers are positioned at a primary source–canceller distance of $r_s = 1{\cdot}715$ m (2λ).

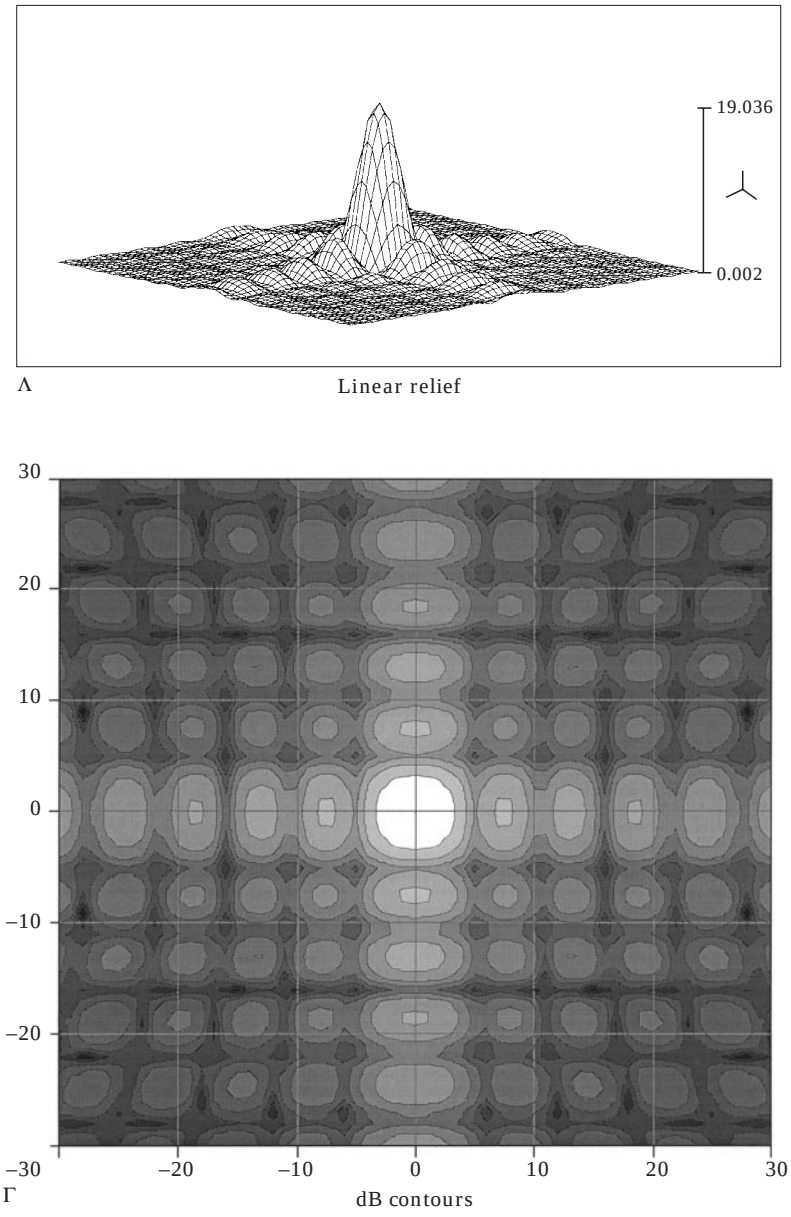

Figure 4(d). $f = 1600$ Hz.

Figure 4. The effect of the source frequency on the directivity pattern ($D = 2$ m, $p = 40 \times 40$, $\theta_o = 60^\circ \times 60^\circ$, $r_o = 50$ m). (a) $f = 200$ Hz; (b) $f = 400$ Hz; (c) $f = 800$ Hz; (d) $f = 1600$ Hz.

A matrix of 3×3 monitoring microphones are equi-spaced within the control angle positioned at 50 m from the primary source. The primary source is represented by $p = 40 \times 40 = 1600$ equi-spaced point sources. The phase and amplitude of the cancellers are optimized to give minimum collective sound pressure at the microphones, by using the method of least squares. Further details of the shadow generating process can be found in reference [1].

System parameters:

$p = 12 \times 12$ $r_M = r_o = 50$ m

$f = 200$ Hz $\lambda = 1.715$ m

$\lambda/D = 0.858$ $\lambda/d = 9.433$

Primary sources positions in space:

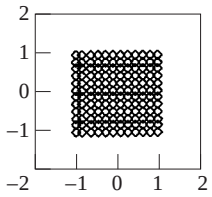

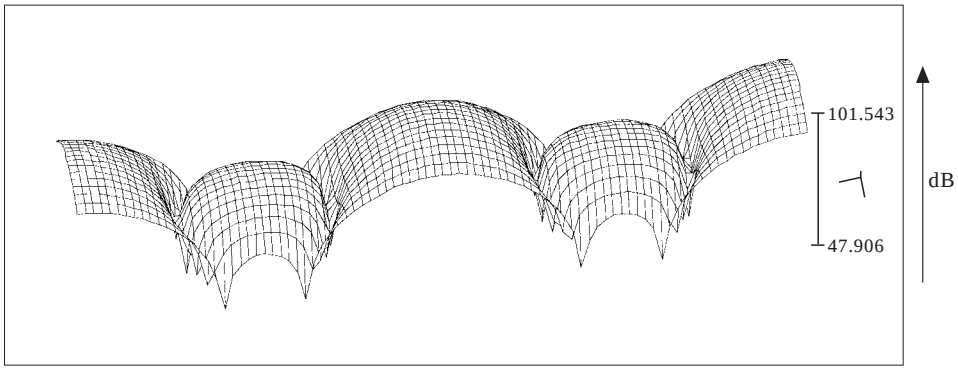

Γ (i) dB relief

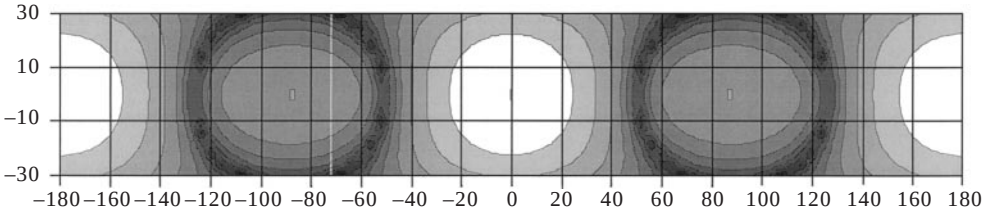

Γ (ii) dB contours

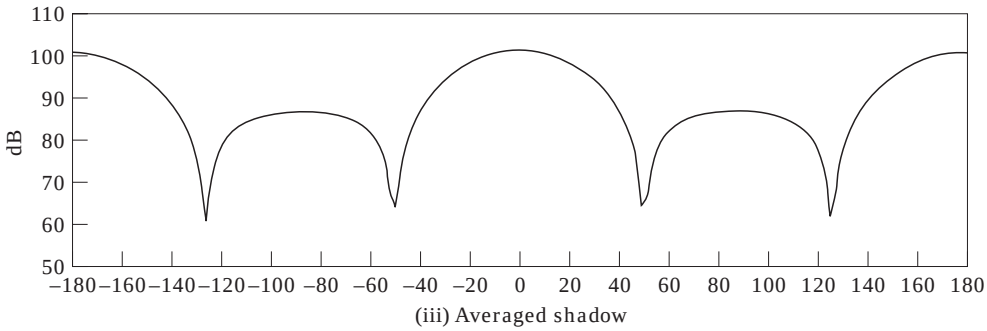

(iii) Averaged shadow

Figure 5(a). $f = 200$ Hz.

System parameters:

$p = 12 \times 12$ $r_M = r_o = 50$ m

$f = 400$ Hz $\lambda = 0.858$ m

$\lambda/D = 0.429$ $\lambda/d = 4.716$

Primary sources positions in space:

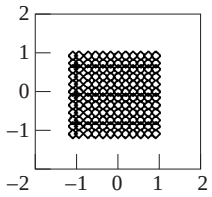

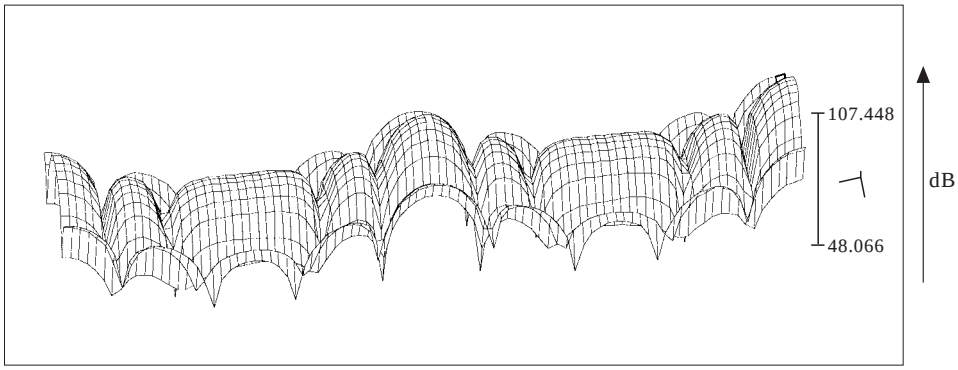

Γ (i) dB relief

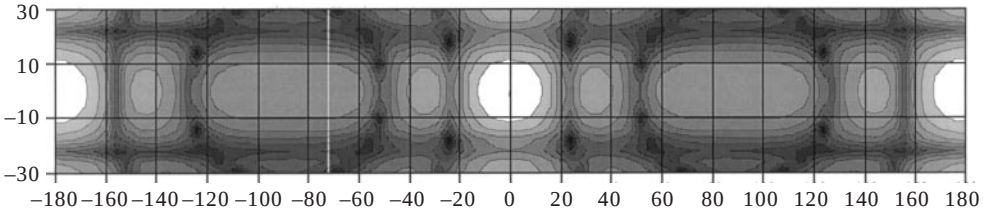

Γ (ii) dB contours

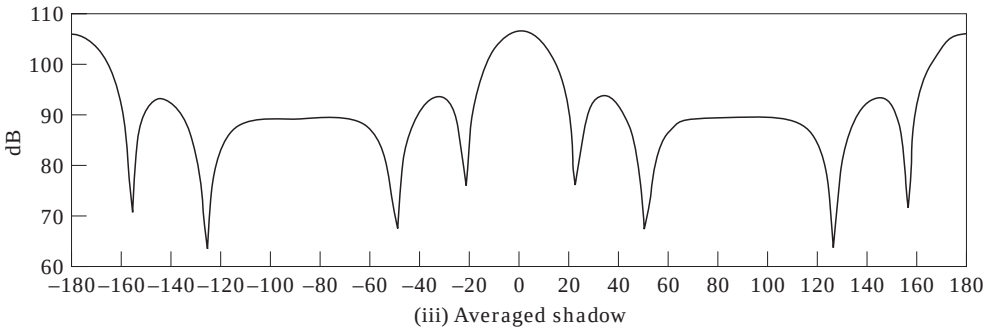

(iii) Averaged shadow

Figure 5(b). $f = 400$ Hz.

System parameters:

$p = 12 \times 12$ $r_M = r_o = 50$ m

$f = 800$ Hz $\lambda = 0.429$ m

$\lambda/D = 0.214$ $\lambda/d = 2.358$

Primary sources positions in space:

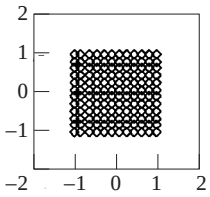

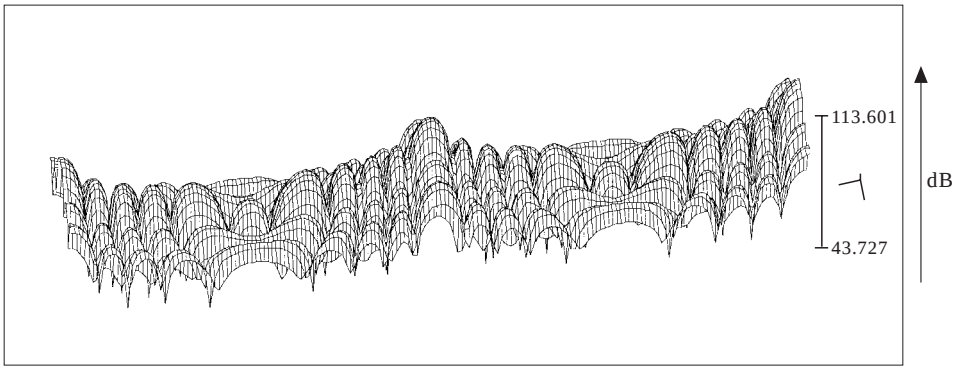

Γ (i) dB relief

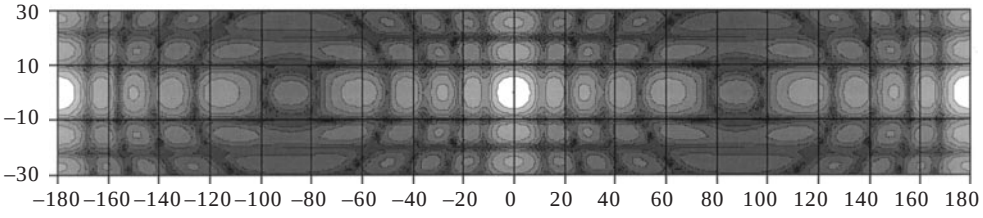

Γ (ii) dB contours

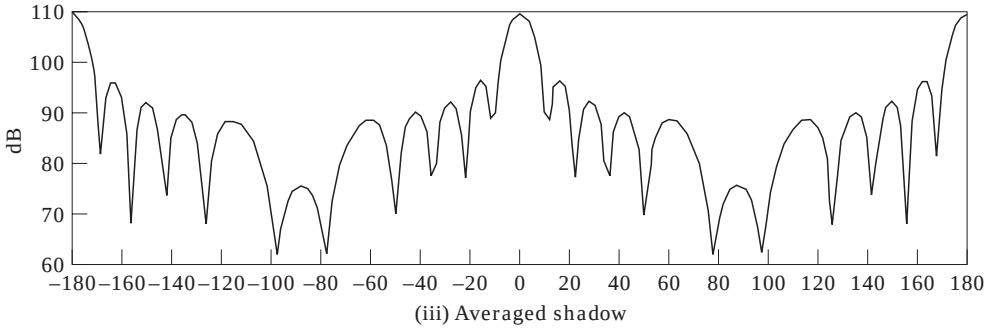

(iii) Averaged shadow

Figure 5(c). $f = 800$ Hz.

System parameters:

$p = 12 \times 12$ $r_M = r_o = 50$ m

$f = 1.6 \times 10^3$ Hz $\lambda = 0.214$ m

$\lambda/D = 0.107$ $\lambda/d = 1.179$

Primary sources positions in space:

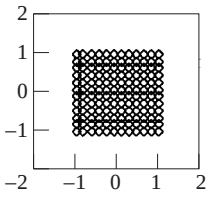

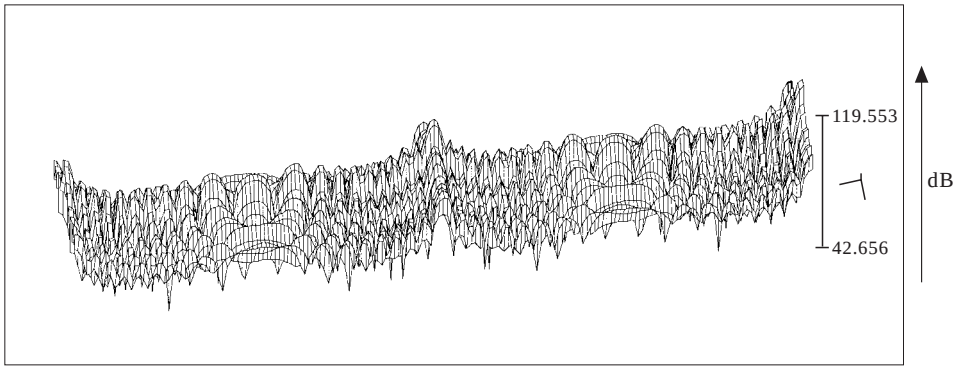

Γ (i) dB relief

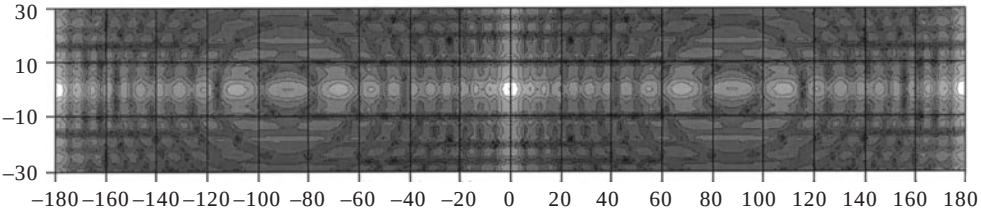

Γ (ii) dB contours

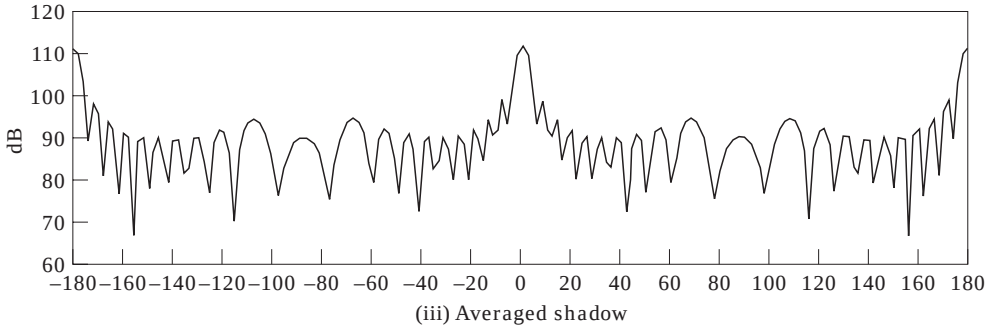

(iii) Averaged shadow

Figure 5(d). $f = 1600$ Hz.

Figure 5. The 360° uncancelled field. (a) $f = 200$ Hz; (b) $f = 400$ Hz; (c) $f = 800$ Hz; (d) $f = 1600$ Hz.

System parameters:

$p = 12 \times 12$ $S = M = 3 \times 3$ $f = 400$ Hz $\lambda = 0.858$ m

$r_S = 1.715$ m (2λ) $r_M = r_o = 50$ m

$\lambda/D = 0.429$ $\lambda/d = 0.858$

Shadow angles: $\alpha_{sh} = 15°$ (azimuth), $\beta_{sh} = 15°$ (elevation)

Microphones and secondary sources positions in space:

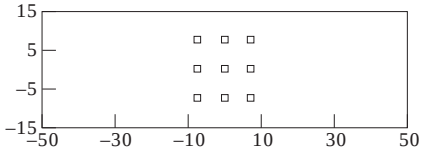

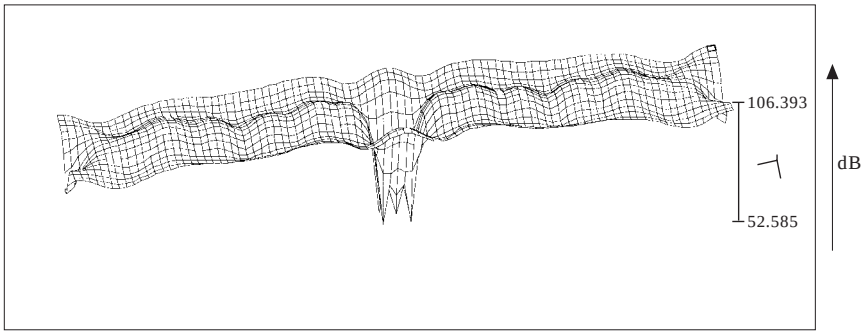

Γ (i) dB relief

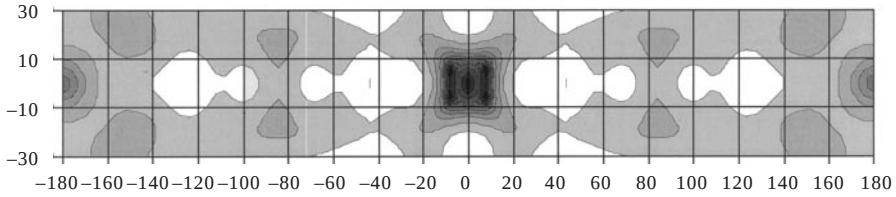

Γ (ii) dB contours

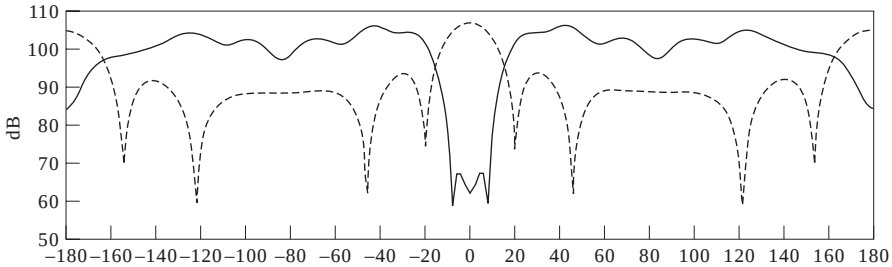

(iii) Averaged shadow

Figure 6(a). 360° shadow details.

In Figures 6(a) (i) and (ii) are shown the resulting shadow in dB relief and dB contour for a 360° observer strip around the primary source, and 60° in elevation. In Figure 6(a) (iii) is shown the shadow averaged across the 15° elevation control angle. The dotted curve shows the uncancelled field with a maximum central SPL of 108 dB and a first zero at $\theta_{z1} = \sin^{-1} \lambda/D = 25°$. A shadow depth of approximately 40 dB, averaged over 15°, is shown.

Radiation is reduced to the rear ($\pm 180°$), as is to be expected for an equal number of half-wavelength primary source–canceller distances. Radiation to the side $\pm(20°$

System parameters:

$p = 12 \times 12$ $S = M = 3 \times 3$ $f = 400$ Hz $\lambda = 0.858$ m

$r_S = 1.715$ m (2λ) $r_M = r_o = 50$ m

$\lambda/D = 0.429$ $\lambda/d = 0.858$

Shadow angles: $\alpha_{sh} = 15°$ (azimuth), $\beta_{sh} = 15°$ (elevation)

Microphones and secondary sources positions in space:

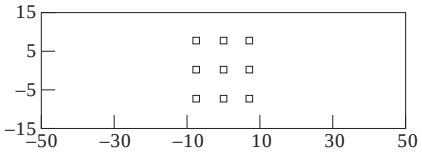

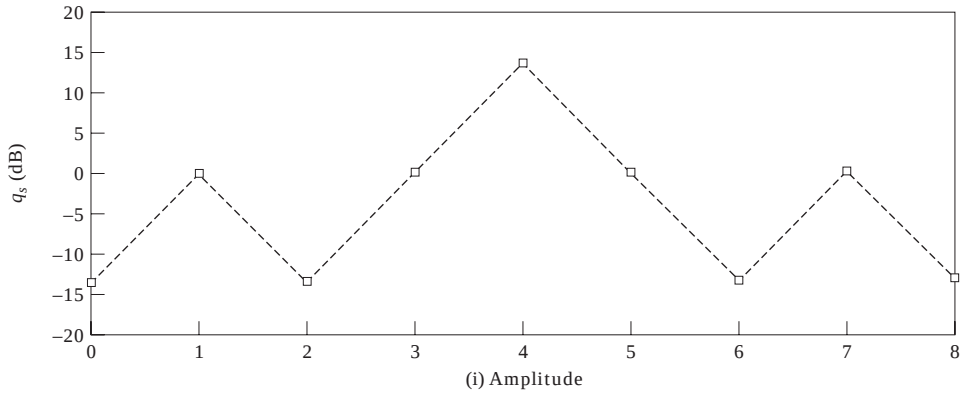

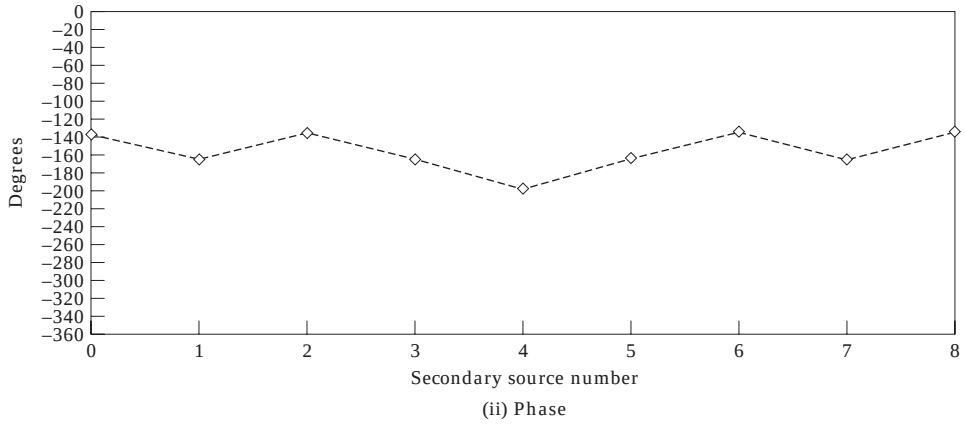

Figure 6(b). Optimized secondary sources.

to 160°) is increased, approaching the maximum uncancelled primary field value. This is to be expected, as the cancelling sources have to generate the opposite but equal magnitude field to cancel the primary field. As the point sources are omnidirectional and not phase coordinated outside the control angle, appreciable sound will be generated to the side. This can be removed by using directional or layered cancelling sources.

In Figure 6(b) are shown the amplitude and phase of the three rows by three columns of cancelling sources (numbered from top right to bottom left). It can be seen that

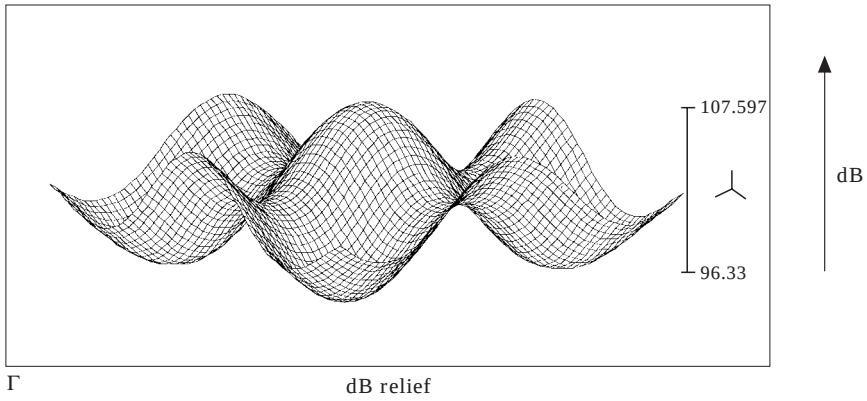

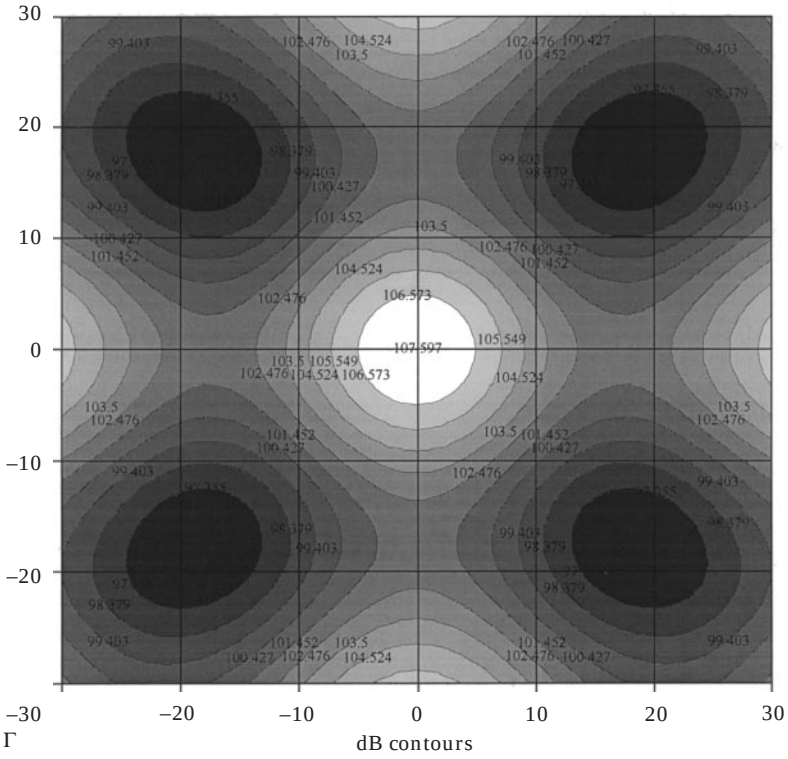

Figure 6(c). Antishadow.

the canceller in the centre of the source array is the most active. Here $q_s = 0{\cdot}5\ \mathrm{m}^3/\mathrm{s}$, or relative to the standard secondary source strength q_{ss}, where $Q_p = 1\ \mathrm{m}^3/\mathrm{s}$ and $S = 9$,

$$q_{ss} = \frac{Q_p}{s} = \tfrac{1}{9}\mathrm{m}^3/\mathrm{s}, \qquad q_s/q_{ss} = 4{\cdot}5, \qquad 20 \log (q_s/q_{ss}) = 13\ \mathrm{dB}. \tag{9}$$

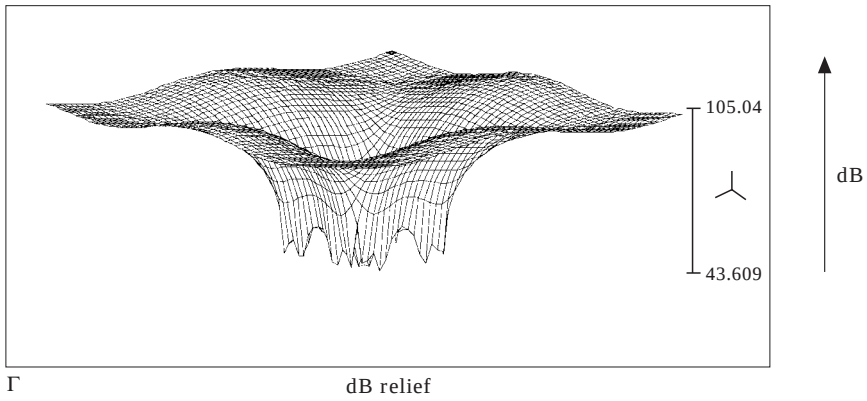

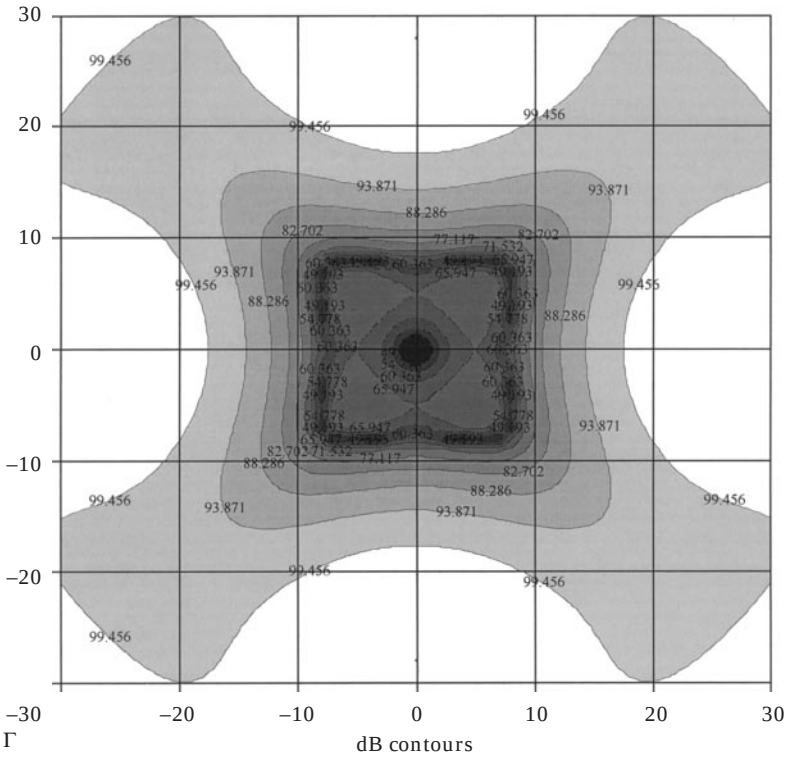

Figure 6(d). Residual field (shadow).

Figure 6. The $15^\circ \times 15^\circ$ standard shadow ($D = 2$ m, $f = 400$ Hz, $\theta_o = 60^\circ \times 60^\circ$, $r_o = 50$ m, $p = 12 \times 12$, $s = 3 \times 3$). (a) 360° shadow details; (b) optimized secondary sources; (c) antishadow; (d) residual field (shadow).

The cancellers in the middle of the array sides have normal strength (0 dB), and the canceller strengths at the corners of the array are almost 15 dB down. The corresponding phases vary between -200° for the centre canceller and -130° at the corners.

In Figure 6(c) is shown the antishadow-optimized canceller field alone (without the primary source field). The two fields in combination generate the residual field (shadow). Note that the central maximum has an exact antipressure of 107·6 dB to cancel the 107·6 dB positive field. Note also that only the centre $15^\circ \times 15^\circ$ of the $60^\circ \times 60^\circ$ sector is being controlled. The uncontrolled surrounding area (interesting square shapes in the corners) is a by-product of the $15^\circ \times 15^\circ$ controlled field. In Figure 6(d) are shown the details of the resulting 40 dB averaged shadow. It is fascinating to observe that two smooth circular-like fields (positive primary and negative secondary) produce a residual sharp rectangular shadow with a basically flat bottom (apart from low values near the microphones going down to 43·7 dB).

4.3. $60^\circ \times 15^\circ$ SHADOW

In Figure 7 is shown a $60^\circ \times 15^\circ$, 400 Hz shadow generated by three rows of nine cancellers, equally spaced over 60° azimuth, 15° elevation controlled angles. This gives the same discreteness factor as the $15^\circ \times 15^\circ$ shadow; i.e., $\lambda/d = 0{\cdot}858$. Other details are the same as in Figure 6. In Figure 7(a) is shown the 60° azimuthal control angle crossing a complex uncancelled primary field, with zeros around $\pm 20^\circ$. As can be seen, the resulting shadow averaged across the 15° elevation angle is 50 dB deep and has no problem traversing the complex field. Radiation behind (180°) is again reduced. Radiation to the side is increased, approaching that of the maximum uncancelled primary source field.

In Figure 7(b) it is again shown that the maximum source strength is in the centre of the canceller array ($q_s \approx 20$ dB), with cancellers on the top and bottom rows having strengths between $+5$ dB and -10 dB. The levels at the corners are 25 dB down. The phase is now showing alternate values of about 80° for adjacent cancellers varying between -200° and -120°, with an average of about -160° for the centre cancellers. The phase approaches -320° ($+40^\circ$) for cancellers at the vertical edges of the canceller array.

In Figure 7(c) are shown details of the antishadow, controlled over $60^\circ \times 15^\circ$. The antishadow across the 60° azimuth angle now resembles the negative of primary field shown in Figure 4(b), including the zeros at approximately $\pm 22^\circ$. This is surprising considering that the secondary field is not controlled outside $\pm 7{\cdot}5^\circ$ in elevation. Again, the maximum sound pressure of the antifield is 107·6 dB, needed to cancel the primary field. Finally, in Figure 7(d) are shown details of the resulting shadow; the residual field is a well formed $60^\circ \times 15^\circ$, 50 dB averaged flat bottomed shadow (with levels near the microphones going down to 23·8 dB).

4.4. $60^\circ \times 15^\circ$ NEAR PERFECT SHADOW

In Figure 8 is shown a $60^\circ \times 15^\circ$, 400 Hz shadow generated by five rows of 13 cancellers, giving a discreteness factor of $\lambda/d = 1{\cdot}715$. In Figure 8(a) is shown a deep 80 dB shadow, with reduced radiation to the rear and excessive radiation (131 dB) to the side. In Figure 8(b) are shown maximum source strengths of 30 dB in the centre rows 1, 3 and 5 and maximum levels of 50 dB ($4{\cdot}6\ m^3/s$ per canceller) in rows 2 and 4. The source strengths at the vertical edges are about -20 dB.

The phase now exhibits $\approx 180^\circ$ phase reversals for alternate cancellers. In fine tuning, the cancellers are obviously "fighting" each other in striving to produce the perfect shadow. In this situation the cancellers are grossly inefficient, generating canceller strengths in excess of 300 times the standard value. The excessive canceller strengths with alternate phases explain the excessive >20 dB side radiation.

System parameters:

$p = 12 \times 12$ $S = M = 9 \times 3$ $f = 400$ Hz $\lambda = 0.858$ m

$r_S = 1.715$ m (2λ) $r_M = r_o = 50$ m

$\lambda/D = 0.429$ $\lambda/d = 0.858$

Microphones and secondary sources positions in space:

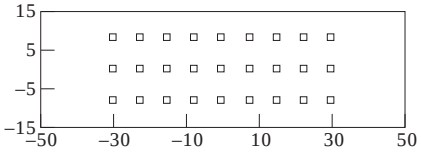

Shadow angles: $\alpha_{sh} = 60°$ (azimuth), $\beta_{sh} = 15°$ (elevation)

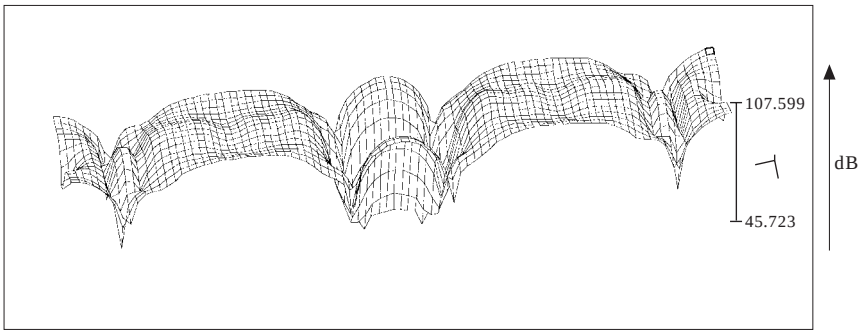

Γ (i) dB relief

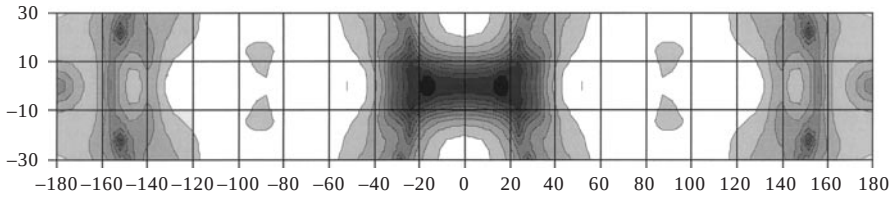

Γ (ii) dB contours

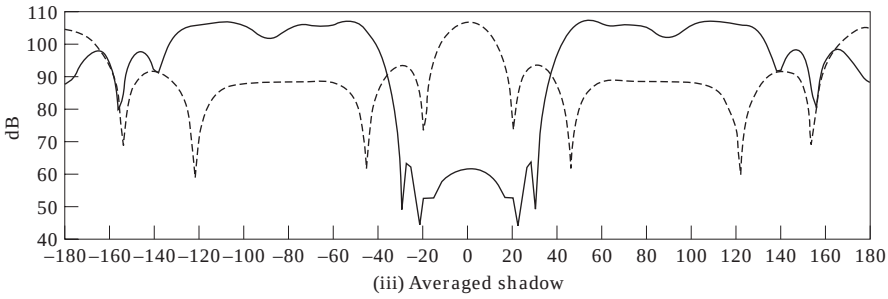

(iii) Averaged shadow

Figure 7(a). 360° shadow details.

In Figure 8(c) are shown the results of the peculiar phenomena of alternate canceller phasing—an almost perfect antishadow as compared with the positive primary field, shown in Figure 10(b), again with a maximum level of 107·6 dB. Although the control is only $\pm 7{\cdot}5°$ in elevation, the remarkable fact is that the antishadow is also being constructed complete with zeros outside these control angles at about 18° in elevation. In Figure 8(d) are shown the details of the resulting $60° \times 15°$ shadow, having an 80 dB averaged shadow bottom.

System parameters:

$p = 12 \times 12$ $S = M = 9 \times 5$ $f = 400$ Hz $\lambda = 0.858$ m

$r_S = 1.715$ m (2λ) $r_M = r_o = 50$ m

$\lambda/D = 0.429$ $\lambda/d = 0.858$

Shadow angles: $\alpha_{sh} = 60°$ (azimuth), $\beta_{sh} = 15°$ (elevation)

Microphones and secondary sources positions in space:

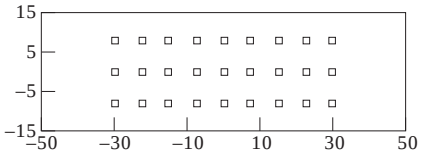

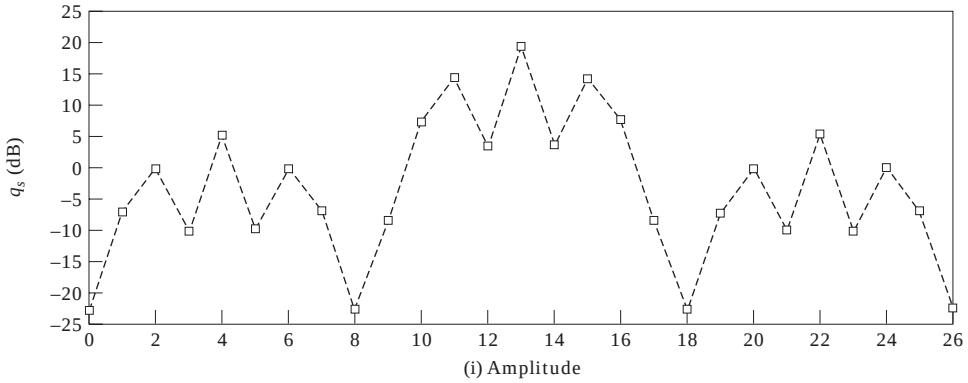

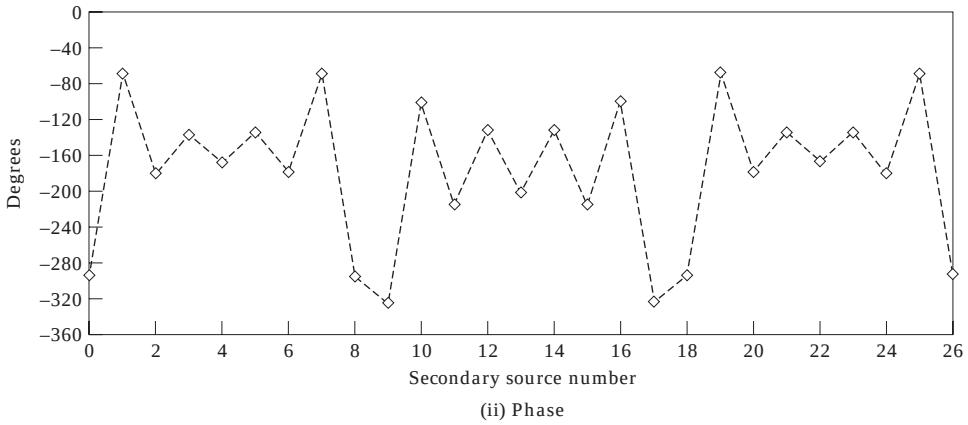

Figure 7(b). Optimized secondary sources.

4.5. 15°, 30° AND 60° SHADOWS

In Figure 9 is shown the construction of 15°, 30° and 60°, 400 Hz shadows using one, two and four 15° × 15° unit shadows for discreteness factors, $\lambda/d = 0{\cdot}858$, $1{\cdot}287$ and $2{\cdot}145$. These were generated by using three, five and nine columns by three, four and five rows, respectively. It can be seen that the construction of arbitrary shadow sizes, using additions of 15° × 15° unit shadows, appears to be valid at this frequency.

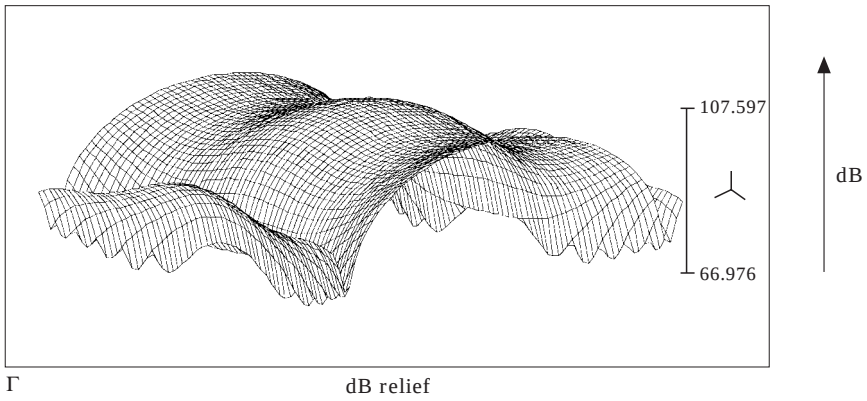

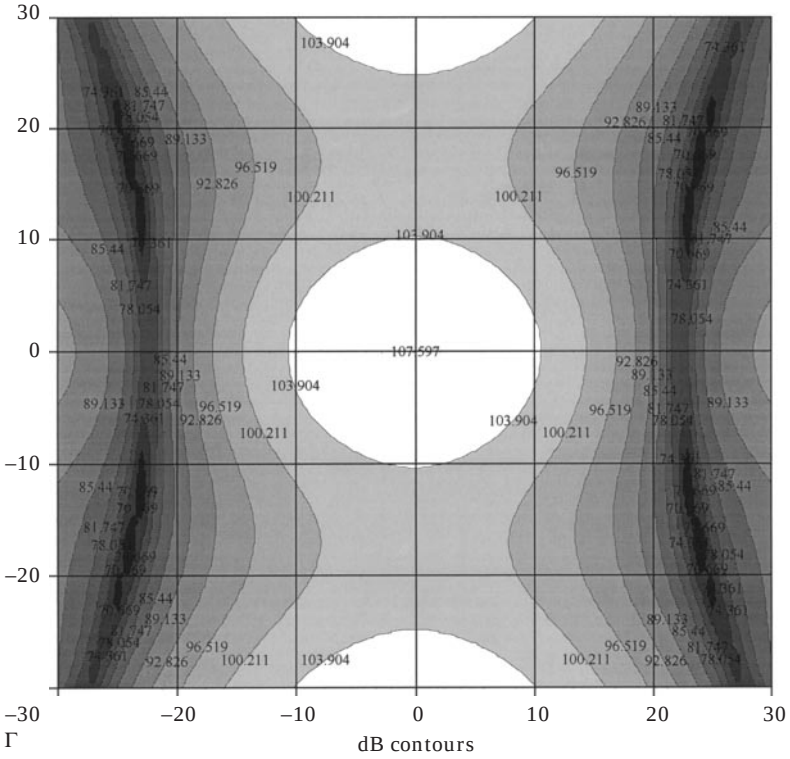

Figure 7(c). Antishadow.

Shadow depths of approximately 40 dB, 45 dB and 75 dB are formed for the three increasing canceller densities. Note that the canceller array with the even number of rows produces only marginally more attenuation than the previous lower canceller density with an odd number of rows. Radiation to the side increases with azimuth angle and canceller density.

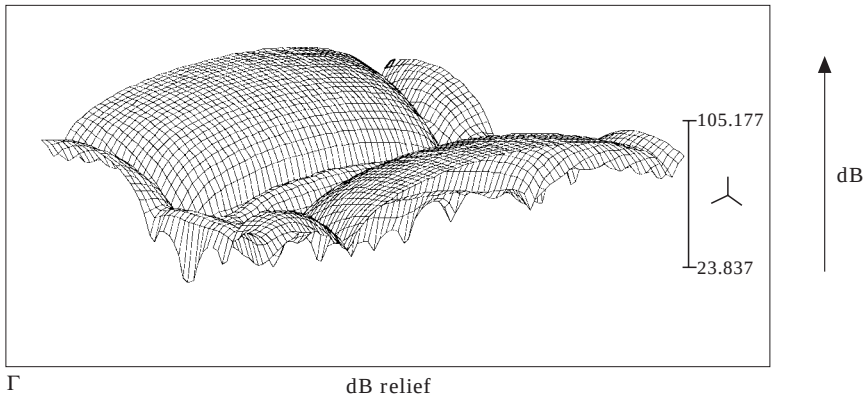

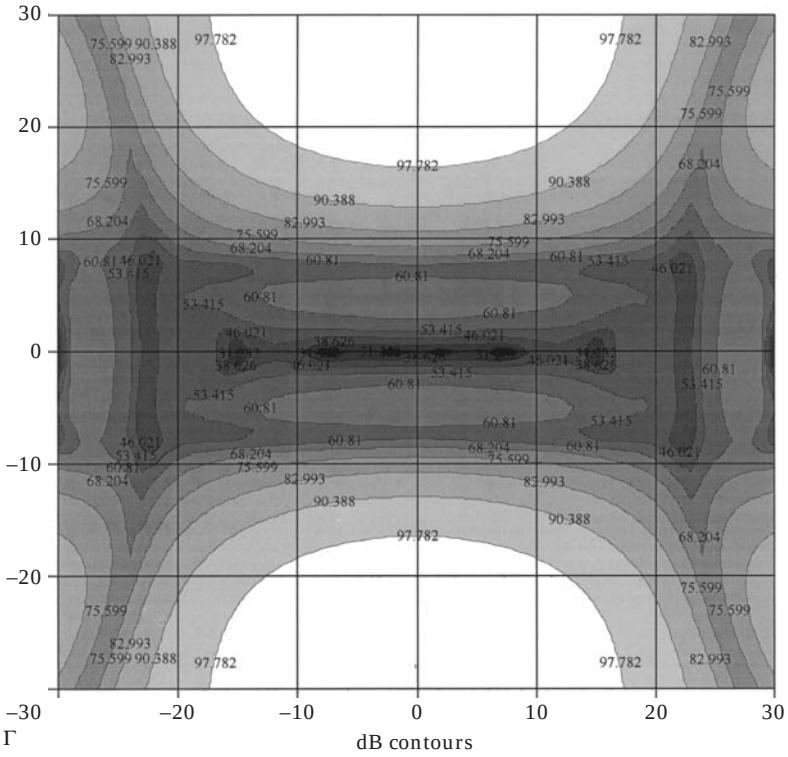

Figure 7(d). Residual field (shadow).

Figure 7. Details of the $60^\circ \times 15^\circ$ shadow ($D = 2$ m, $f = 400$ Hz, $\theta_o = 60^\circ \times 60^\circ$, $r_o = 50$ m, $p = 12 \times 12$; $s = 9 \times 3$). (a) 360° shadow details; (b) optimized secondary sources; (c) antishadow; (d) residual field (shadow).

Microphones and secondary sources positions in space:

System parameters:

$p = 12 \times 12$ $S = M = 13 \times 5$ $f = 400$ Hz $\lambda = 0.858$ m

$r_S = 1.715$ m (2λ) $r_M = r_o = 50$ m

$\lambda/D = 0.429$ $\lambda/d = 1.715$

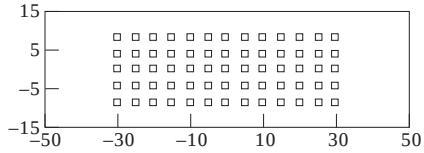

Shadow angles: $\alpha_{sh} = 60°$ (azimuth), $\beta_{sh} = 15°$ (elevation)

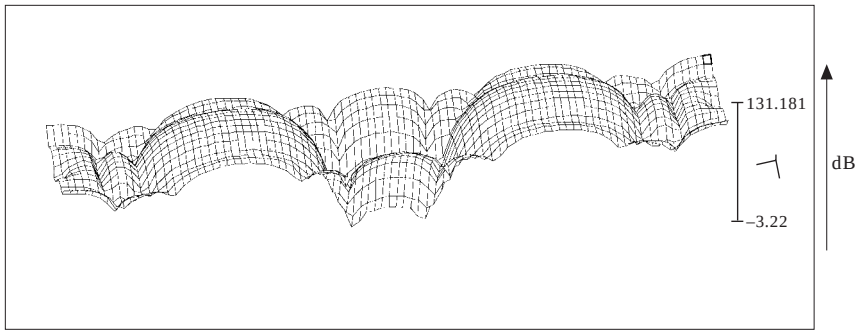

Γ (i) dB relief

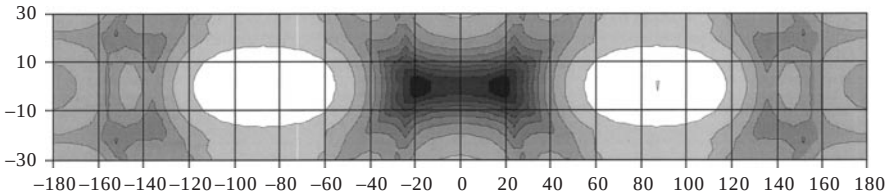

Γ (ii) dB contours

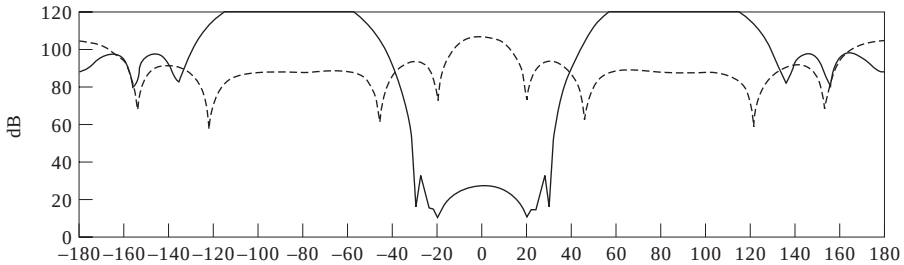

(iii) Averaged shadow

Figure 8(a). 360° shadow details.

4.6. DISTANCE CURVES

In Figure 10 is shown the 15° × 15°, 400 Hz average shadow depth (dB) as a function of microphone distance (r_m) for various observer distances (r_o). Basically, the shadow depth increases with microphone and observer distance from the primary sources. Below 10λ the shadow mechanism does not work effectively (near field and $r_s = 2\lambda$). For microphone distances greater than 100λ, the shadow depth levels off to about 40 dB.

Microphones and secondary sources positions in space:

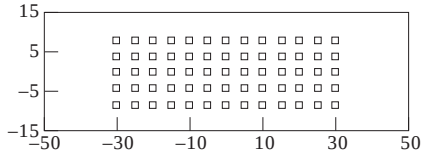

System parameters:

$p = 12 \times 12$ $S = M = 13 \times 5$ $f = 400$ Hz $\lambda = 0.858$ m

$r_S = 1.715$ m (2λ) $r_M = r_o = 50$ m

$\lambda/D = 0.429$ $\lambda/d = 1.715$

Shadow angles: $\alpha_{sh} = 60°$ (azimuth), $\beta_{sh} = 15°$ (elevation)

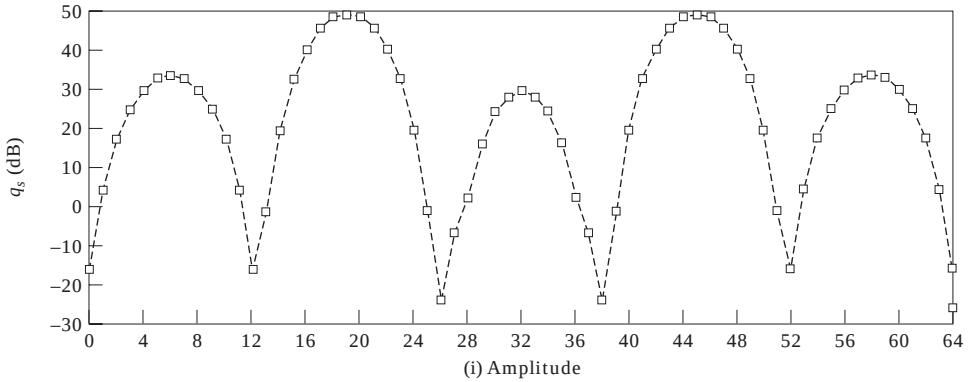

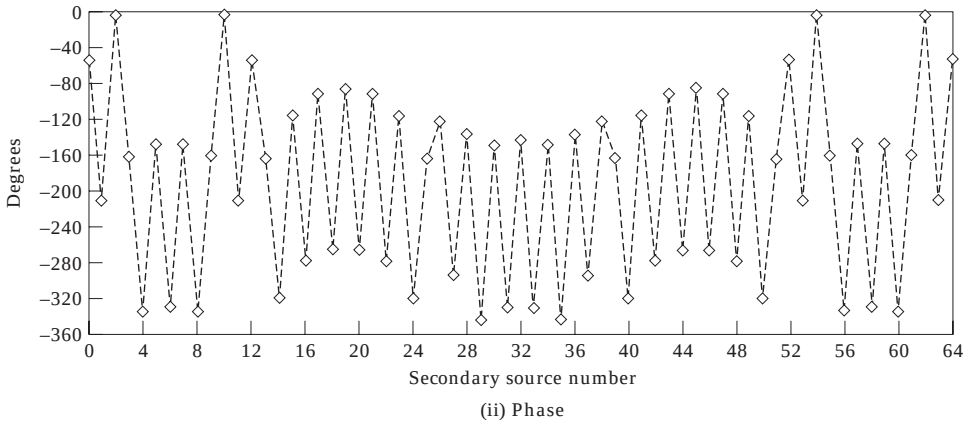

Figure 8(b). Optimized secondary sources.

For large observer distances $r_o > 100\lambda$ and microphone distances r_m between 10λ and 100λ, the shadow depth in dB is given approximately by

$$\text{dB} = -40 \log (r_m/10). \tag{10}$$

The dotted curve gives the level when the observer and microphone are at the same distance $r_o = r_m$. The standard distance $r_o = r_m = 50$ m $(58{\cdot}4\lambda)$ is also shown.

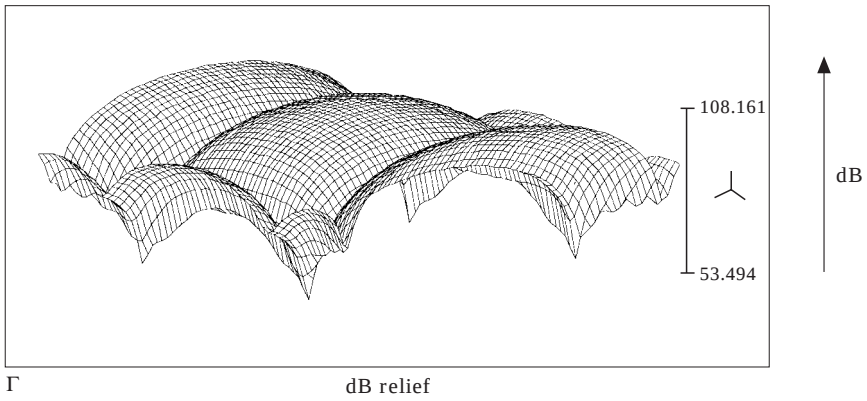

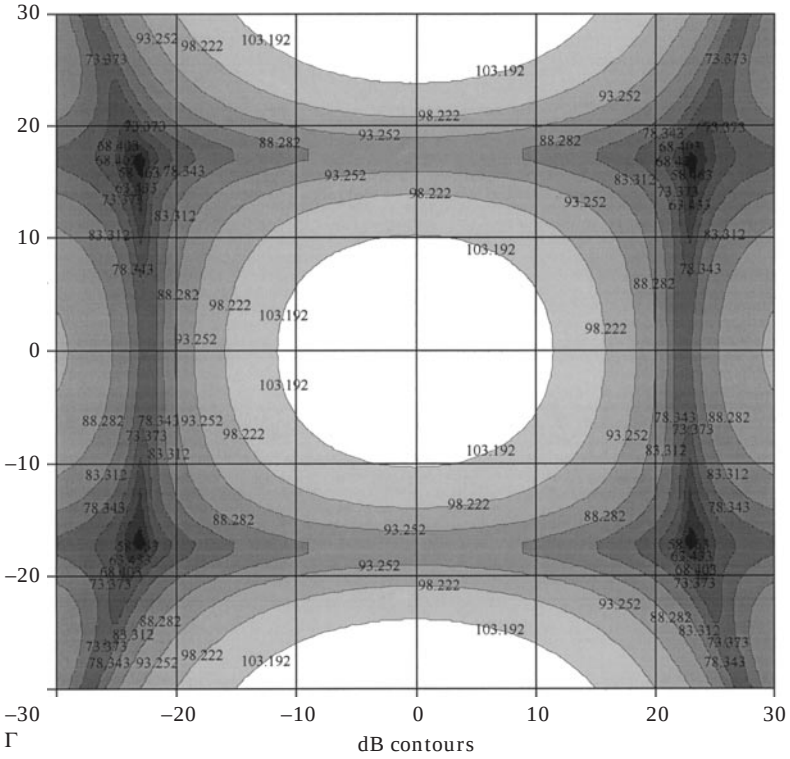

Figure 8(c). Antishadow.

4.7. PERFORMANCE CURVES

In Figure 11 is shown the cancellation performance at 400 Hz for the $15^\circ \times 15^\circ$ unit shadow. The shadow depths are plotted as a function of the discreteness factor λ/d for various canceller distances r_s. The curves are unique for a compactness factor of

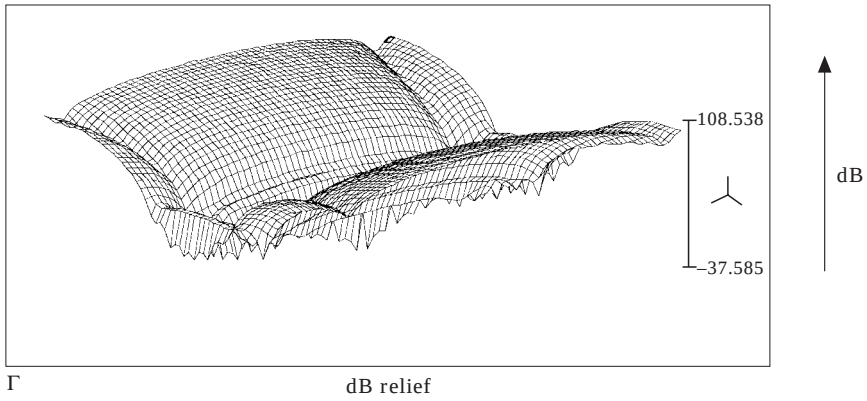

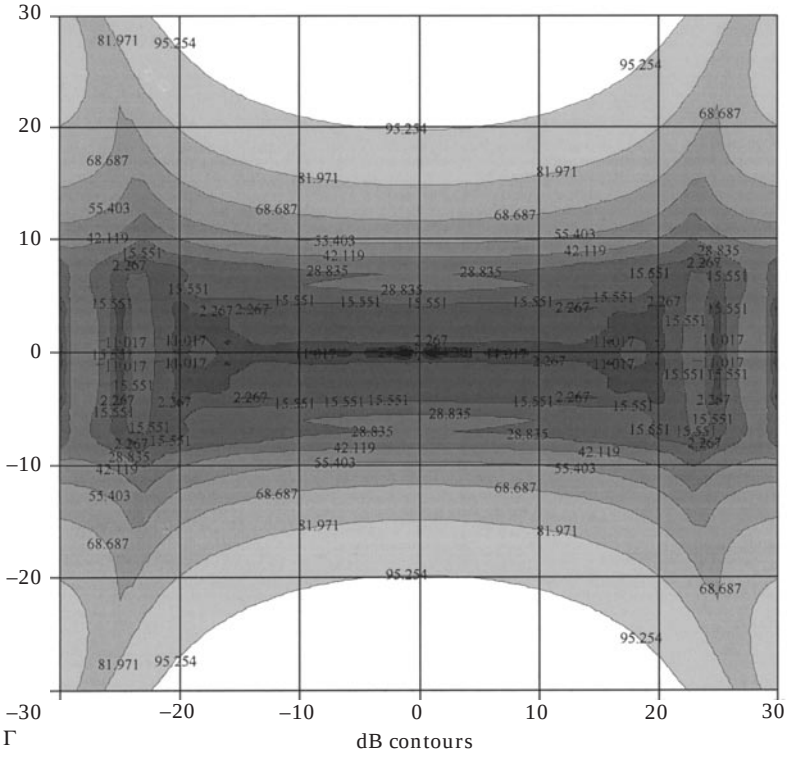

Figure 8(d). Residual field (shadow).

Figure 8. Details of the $60^\circ \times 15$ shadow—high canceller density ($D = 2$ m, $f = 400$ Hz, $\theta_o = 60^\circ \times 60^\circ$, $r_o = 50$ m, $p = 12 \times 12$, $s = 13 \times 5$). (a) 360° shadow details; (b) optimized secondary sources; (c) antishadow; (d) residual field (shadow).

$\lambda/D = 0{\cdot}429$ and for observer and microphone distances both of 50 m ($58{\cdot}4\lambda$). The canceller matrix is shown on the top of the figure. It can be seen that the curves "turn on" at about $\lambda/d = 0{\cdot}5$, and shadows in excess of 100 dB are generated.

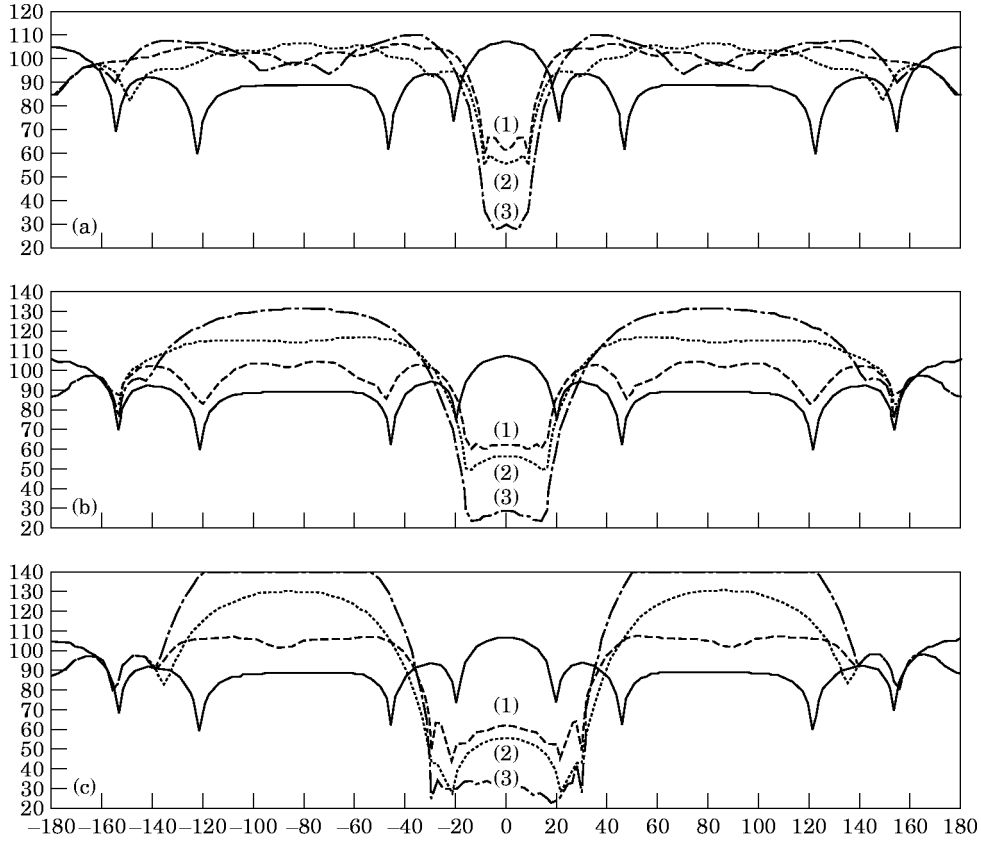

Figure 9. The construction of 15°, 30° and 60° shadows by using one, two and four 15° × 15° unit shadows for various numbers of cancellers ($f = 400$ Hz, $D = 2$ m, $r_s = 2\lambda$). (a) $\alpha = 15°$: $S = 3 \times 3$ (1), $S = 4 \times 4$ (2), $S = 5 \times 5$ (3). (b) $\alpha = 30°$: $S = 5 \times 3$ (1), $S = 7 \times 4$ (2), $S = 9 \times 5$ (3). (c) $\alpha = 60°$: $S = 9 \times 3$ (1), $S = 13 \times 4$ (2), $S = 17 \times 5$ (3).

For matrix densities greater than 6×6, shadows continue to grow in depth, but excessive radiation to the side appears. For shadow depths greater than approximately 120 dB, the cancellation mechanism fails (points contained inside of the box). Note again that even arrays are less efficient than odd arrays (the even arrays do not have the more efficient central rows and columns of cancellers). The data suggests the prediction curves

$$\text{dB} = -n \log 2(\lambda/d), \tag{11}$$

where $n = 9$, 13 and 16 for $r_s = 8\lambda$, 2λ and $\lambda/2$, respectively. Compared with the 100 Hz ($\lambda/D = 1{\cdot}71$) performance curves in reference [1], all other parameters being the same, these higher frequency curves turn on sooner and produce deeper shadows for the same discreteness factor λ/d.

Thus deep shadows are again obtained, even for non-compact sources. For example, Figure 11 predicts that $\sim$40 dB shadows are achievable over a 15° × 15° control angle by using a 3×3 canceller array at 400 Hz over a 2 m square source. Or equivalently, the same shadow depth can be achieved at 3200 Hz over a 0·25 m square source, as can be seen from Table 1 (for the same λ/D and λ/d).

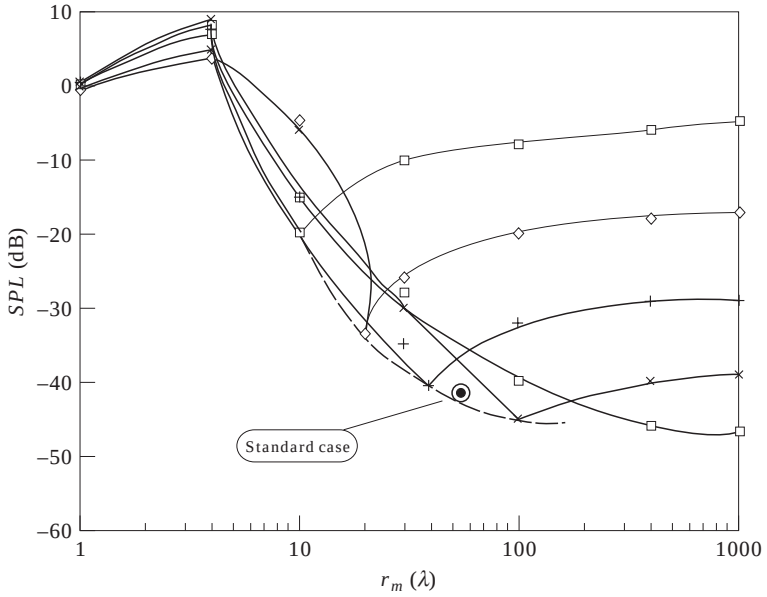

Figure 10. 400 Hz distance curves showing the average shadow depth (dB) as a function of microphone distance $r_m(\lambda)$ for various observer distances $r_o(\lambda)$. r_o/λ: □, 10; ◇, 20; +, 40; ×, 100; □, 1000 ($D = 2$ m, $\lambda = 0{\cdot}858$ m, $r_s = 2\lambda$, $\lambda/D = 0{\cdot}429$, $s = 3 \times 3$, $d = 1$, $\lambda/d = 0{\cdot}858$, $15^\circ \times 15^\circ$ unit shadow.

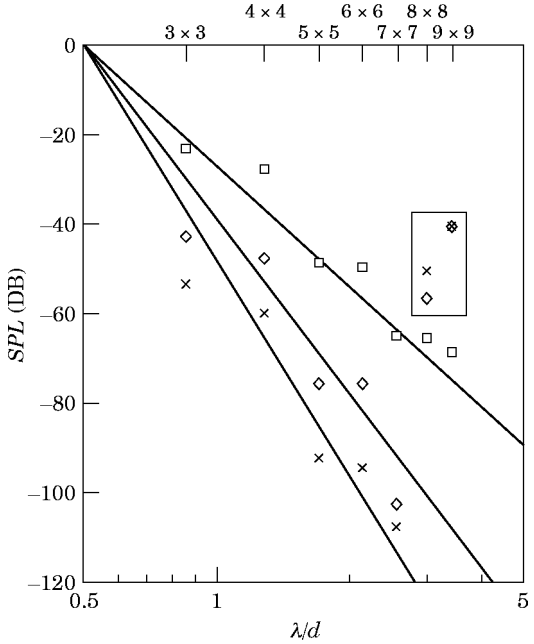

Figure 11. 400 Hz performance curves showing the average shadow depth (dB) as a function of non-dimensionalized canceller spacing (λ/d) for various canceller distances $d_s(\lambda)$: d_s/λ: ×, 1/2; ◇, 2; □, 8. ($D = 2$ m, $\lambda = 0{\cdot}858$ m, $\lambda/D = 0{\cdot}429$, $r_o = r_m = 50$ m ($58{\cdot}4\lambda$), $15^\circ \times 15^\circ$ unit shadow.

5. CONCLUSIONS

The active control of free field radiation from unconfined sources has been investigated. It has been shown that practical shadows are possible when using a modest number of cancellers.

In reference [1], deep acoustic shadows were generated electronically for compact sources; i.e., with a compactness factor $\lambda/D > 1$, where D is the size of the source distribution. In this paper, deep shadows are again obtained, even for a non-compact source ($\lambda/D < 1$), provided that the discreteness factor $\lambda/d > 1$, where d is now the separation distance between cancellers.

Cancellers operating under optimum shadow performance intelligently adjust their phase and strength to give optimum bell shaped secondary source distributions. This removes diffraction effects produced by natural solid barriers, resulting in superior shadows.

REFERENCES

1. S. E. Wright and B. Vuksanovic 1996 *Journal of Sound and Vibration* **190**(3) (E. J. Richards Memorial Issue), 565–585. Active control of environmental noise.
2. Lord Rayleigh 1896 *Theory of Sound*. New York, Dover (1945 reissue). See Vol. 2, 97–148 (Original edition published by the MacMillan Company, 1896.)
3. S. E. Wright 1986 *Journal of Sound and Vibration* **108**, 361–378. Sources and observers in motion, I: time variant analysis and its implications for aerodynamical sound.
4. P. E. Doak 1965 *Proceeding of the Fifth International Congress on Acoustics*, *Liège*, *Paper K*56. Multipole analysis of acoustic radiation.
5. S. G. Starling and A. J. Woodall 1957 *Physics*. London: Longman. See pp. 664–698.
6. F. A. Jenkins and H. E. White 1950 *Fundamentals of Optics*. New York: McGraw-Hill; second edition.
7. R. W. James 1952 *X Ray Crystallography*. London: Methuen; fifth edition.

APPENDIX: THEORETICAL DEVELOPMENT

A1. SINGLE POINT SOURCE

The complex sound pressure $P(r)$ in Pascals at some distance r from a single, monopole point sound source S, acting alone in space, can be calculated by using the equation

$$P(r) = \frac{j\omega\rho}{4\pi r} q\, e^{j(\omega t - kr)}, \tag{A1}$$

where $\omega = 2\pi f$ is the angular frequency of the source in rad/s, ρ is the density of the propagating medium (for air at 20°C, $\rho = 1{\cdot}21$ kg/m^3), q is the complex source strength (m^3/s), $k = \omega/c = 2\pi/\lambda$ is the wavenumber (c is the speed of sound in the propagating medium and λ is the wavelength of the sound waves; for air at 20°C, $c = 343$ m/s), and kr is the phase change with propagation distance in radians. For further details on acoustic sources; see, for example, references [2] and [3].

In the case of a constant frequency f, air density ρ and constant source strength q, with the time dependent factor omitted, the above expression can be written as

$$P(r) = A(r)\, e^{-jkr}, \tag{A2}$$

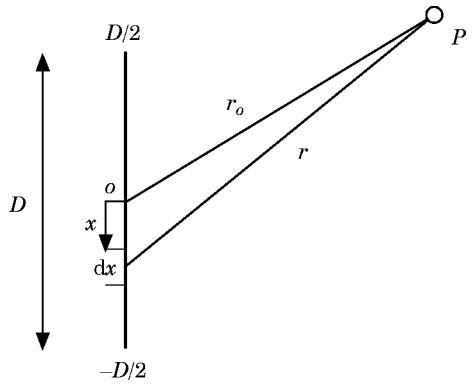

Figure A1. The line source geometry.

where e^{-jkr} is a unit vector rotating with phase angle kr and $A(r)$ is the sound pressure amplitude given by

$$A(r) = (j\omega\rho/4\pi r)q. \tag{A3}$$

A2. CONTINUOUS SOURCE DISTRIBUTION

To calculate the sound pressure $P(r)$ at a distance r from a finite line source of length D, one can divide this source into a large number of small elements of length dx (point sources). According to relations (A2) and (A3) and Figure A1, each of these source elements contributes an incremental sound pressure dP to the overall complex sound pressure at a distance point r, given by

$$dP(r) = A'(r)\,dx\,e^{-jkr}, \tag{A4}$$

where

$$A'(r) = (j\omega\rho/4\pi r)q'. \tag{A5}$$

The total sound pressure from the entire source then becomes

$$P(r) = \int_{-D/2}^{D/2} A'(r)\,e^{-jkr}\,dx, \tag{A6}$$

where r_o is the distance between the mid-point of the source and the observation point P, r is the distance between the source element ds and the observation point P, and q' is the source strength per unit length, $q' = q/D$, in which D is the size of the sound source.

A3. NEAR FIELD

Close to the source, the propagation distance r for each element dx is given below and illustrated in more detail in Figure A2, where AO represents half the source in Figure A1.

One has

$$r = r_o + \Delta r, \qquad \Delta r = AC - \delta r = AB, \tag{A7}$$

$$\delta r = BP - CP, \qquad CP = \sqrt{OP^2 - OC^2}, \tag{A8}$$

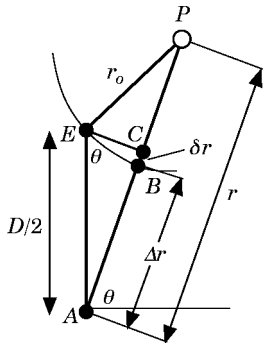

Figure A2. The near field geometry.

$$OC = (D/2)\cos\theta, \qquad OP = BP = r_o, \qquad AC = (D/2)\sin\theta, \tag{A9}$$

$$\Delta r = (D/2)\sin\theta - \delta r, \qquad \delta r = r_o(1 - \sqrt{1 - [(D/2r_o)\cos\theta]^2}). \tag{A10}$$

For the observer close to the source and $\delta r > \lambda$ the full expression, equations (A7) and (A10), have to be used in equation (A6). Upon using $(1 + x)^n \approx 1 + nx$ in equation (A10), one has

$$\delta r \simeq (D^2/8r_0)\cos^2\theta. \tag{A11a}$$

Zeros (or minima) will occur when $\delta r = (\lambda/2) + z\lambda$, giving

$$r_{z1} \simeq (D\cos\theta)^2/8\lambda(\tfrac{1}{2} + z). \tag{A11b}$$

Using the first zero, $z = 0$ (approaching the source), to characterize the extent of the near field (collapse of far field), one has

$$r_{z1} \simeq (D\cos\theta)^2/4\lambda. \tag{A11c}$$

Thus the near field extends out in front of the source, not to the sides ($\cos\theta$ effect). The higher the frequency, or the larger the source size, the further the near field extends. Of course, the onset of the near field will extend much further than this (at least $2r_{z1}$ from the source).

Because the amplitude of sound at the observer, from each source element, varies enormously with x in this region, there is no simple closed form solution. Here, one has to rely on numerical solutions to evaluate equation (A6).

A4. FAR FIELD

For the observer far from the source, δr is always much less than λ, and δr can be neglected; the region is then referred to as the geometric far field. Here, the sound pressure at the observer is relatively constant from each source element and equation (A10) becomes:

$$\Delta r \simeq (D/2)\sin\theta. \tag{A12}$$

Assuming far field conditions, and neglecting small changes in r in the denominator of expression (A5) as being insensitive compared to those in the exponential term, one can replace r by r_o. The term $A'(r)$ is then replaced with $A'(r_o)$ and considered constant in the

integration. The complex sound pressure at r_o can then be calculated from equations (A6), (A7) and (A12) as

$$P(r_o) = A'(r_o) \int_{-D/2}^{D/2} e^{-jk(r_o + x \sin\theta)}\, dx = A'(r_o) \int_0^{D/2} e^{-jk(r_o - x \sin\theta)} + e^{-jk(r_o + x \sin\theta)}\, dx, \quad \text{(A13a)}$$

and using $\cos x = (e^{jx} + e^{-jx})/2$ gives

$$P(r_o) = 2A'(r_o)\, e^{-jkr_o} \int_0^{D/2} \cos(kx \sin\theta)\, dx, \quad \text{(A13b)}$$

which can be written as

$$P(r_o) = A'(r_o)D\, e^{-jkr_o}\chi_c = A(r_o)\, e^{-jkr_o}\chi_c, \quad \text{(A14)}$$

where $A(r_o) = A'(r_o)D$ becomes the total sound pressure amplitude and

$$\chi_c = (\sin\gamma)/\gamma, \qquad \gamma = (kD \sin\theta)/2 = \pi D \sin\theta/\lambda. \quad \text{(A15)}$$

A5. NON-COMPACT SOURCES

The interference function $|\chi_c|$ which takes account of the acoustic interference across a continuous source distribution is shown in Figure A3. The zero order maximum of the function $|\chi_c|$ is given when $\gamma = 0$; when D is very small compared with λ, then $|\chi_c|$ becomes

$$|\chi_c| = \lim_{\gamma \to 0} |(\sin\gamma)/\gamma| = \lim_{\gamma \to 0} |\cos\gamma| \to 1. \quad \text{(A16)}$$

Here, there is no interference and the source is said to be compact, or equivalent to a point source. Higher order maxima of the function $|\chi_c|$ are given when

$$\gamma = (2n + 1)\pi/2, \qquad \text{where } n = 1, 2, \ldots. \quad \text{(A17)}$$

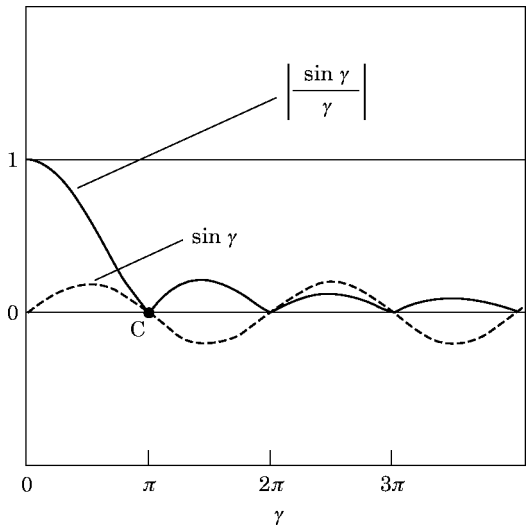

Figure A3. The continuous interference function $|\chi_c|$.

From equations (A15) and (A17), and for $n = 1$, the first maximum is given by

$$\gamma = (\pi D \sin \theta_{n1})/\lambda = 3\pi/2 \qquad \text{or} \qquad \theta_{z1} = \sin^{-1}(3\lambda/2D). \tag{A18}$$

The function $|\chi_c|$ has zeroes when

$$\gamma = z\pi, \qquad \text{where } z = 1, 2, \ldots. \tag{A19}$$

Of particular interest is the first zero ($z = 1$) indicated by point C on Figure A3. This zero, according to equations (A15) and (A19), corresponds to an angle θ_{z1} given by

$$\gamma = (\pi D \sin \theta_{z1})/\lambda = \pi \qquad \text{or} \qquad \theta_{z1} = \sin^{-1}(\lambda/D). \tag{A20}$$

Using this zero, one can now define a non-compact source with dimension D such that the first zero of the function $|\chi_c|$ occurs for $\theta \leqslant 90^\circ$, giving

$$D \geqslant \lambda. \tag{A21}$$

Thus a non-compact source can be defined as one for which the source dimension is larger than the acoustic wavelength. Here $\chi < 1$ and the acoustic interference across the finite distribution reduces the total sound pressure compared with that of a compact source with the same source strength. This interference effect is equivalent to Fraunhofer diffraction across a slit in optics.

A6. MULTI-DIMENSIONAL SOURCES

For a two orthogonal dimensional source one can anticipate that there will be the equivalent of two χ functions, one for each dimension as depicted in Figure A4. Here functions χ_{cx} and χ_{cy} are of the same type as above, where θ_x and θ_y are now the angles of the planes containing the observer radius vector and the y and x co-ordinate axes, respectively, make the surface normal (z-axis), as shown in Figure A4. In this case

$$P(r_o) = A(r_o)\, \mathrm{e}^{-\mathrm{j}kr_o} \chi_{cx} \chi_{cy}, \tag{A22}$$

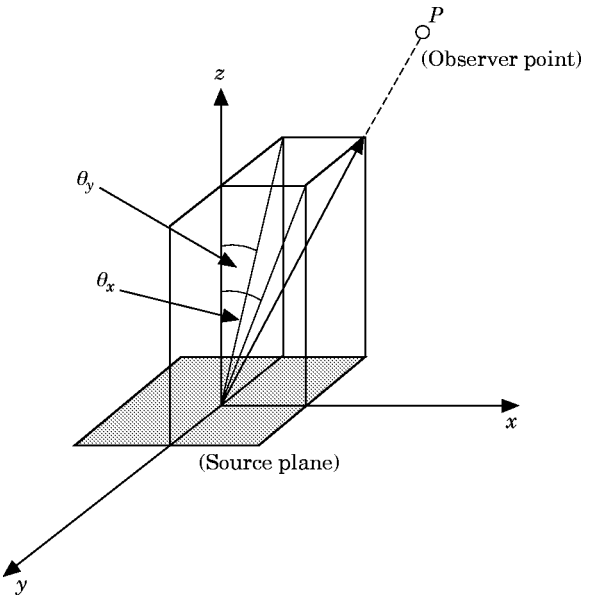

Figure A4. The two-dimensional source geometry.

where

$$\chi_{cx} = \left[\sin\left(\frac{ka \sin\theta_x}{2}\right) \Big/ \left(\frac{ka \sin\theta_x}{2}\right) \right], \tag{A23}$$

$$\chi_{cy} = \left[\sin\left(\frac{kb \sin\theta_y}{2}\right) \Big/ \left(\frac{kb \sin\theta_y}{2}\right) \right]. \tag{A24}$$

For a circular source, the two χ functions combine to form a single Bessel function, such as that found in describing the interference across a loudspeaker diaphragm.

In the case of a three-dimensional source, a further equivalent function χ_c will be in operation for the third dimension. For further information on acoustic interference from finite acoustic source distributions, see, for example, reference [4].

A7. TWO POINT SOURCES

For the case of two point sound sources, the complex sound pressure at point P can be calculated by using the superposition principle as

$$P(r) = P(r_1) + P(r_2), \tag{A25}$$

where $P(r_1)$ and $P(r_2)$ are complex sound pressures at the observer point from sources S_1 and S_2 respectively. Upon using equation (A1) this becomes

$$P(r) = (\mathrm{j}\omega\rho/4\pi r_1)q\ \mathrm{e}^{-\mathrm{j}kr_1} + (\mathrm{j}\omega\rho/4\pi r_2)q\ \mathrm{e}^{-\mathrm{j}kr_2}. \tag{A26}$$

For far field conditions, i.e., $r \gg d^2/4\lambda$, from equation (A11c), where d is now the separation distance between the sources, one can assume that $r_1 \approx r_2 \approx r_o$ in the denominator, making

$$(\mathrm{j}\omega\rho/4\pi r_1)q \approx (\ \mathrm{j}\omega\rho/4\pi r_2)q \approx (\mathrm{j}\omega\rho/4\pi r_o)q = A(r). \tag{A27}$$

However retaining the more sensitive differences between r_1 and r_2 in the exponential term gives

$$P(r_o) = A(r)(\mathrm{e}^{-\mathrm{j}kr_1} + \mathrm{e}^{-\mathrm{j}kr_2}) = A(r_o)\,\mathrm{e}^{-\mathrm{j}kr_o}(1 + \mathrm{e}^{-\mathrm{j}k\Delta r}), \tag{A28}$$

where the path difference in the far field between sources is given by equation (A12) as

$$r_2 - r_1 = \Delta r = d \sin\theta. \tag{A29}$$

Expression (A28) now becomes

$$P(r_o) = A(r)\,\mathrm{e}^{-\mathrm{j}kr_o}|\chi_d|, \tag{A30}$$

where

$$\chi_d = 1 + \mathrm{e}^{-\mathrm{j}\gamma}, \qquad \gamma = k\Delta r = (2\pi d \sin\theta)/\lambda. \tag{A31}$$

The first zero of the discrete interference function $|\chi_d|$ occurs for $\gamma = \pi$: i.e., for $\sin\theta = \lambda/2d$. Therefore a two-point discrete source can be considered non-compact according to the previously given definition, i.e., $\theta \leqslant 90^\circ$, giving

$$d \geqslant \lambda/2. \tag{A32}$$

A8. N POINT SOUND SOURCES IN LINEAR ARRAY

In the case of N point sound sources arranged in a linear array as depicted in Figure A5, expression (A28) for the complex sound pressure becomes

$$P(r_o) = A(r)\,\mathrm{e}^{-\mathrm{j}kr_o}(1 + \mathrm{e}^{-\mathrm{j}k\Delta r} + \mathrm{e}^{-\mathrm{j}k2\Delta r} + \mathrm{e}^{-\mathrm{j}k3\Delta r} + \cdots + \mathrm{e}^{-\mathrm{j}k(N-1)\Delta r}), \tag{A33}$$

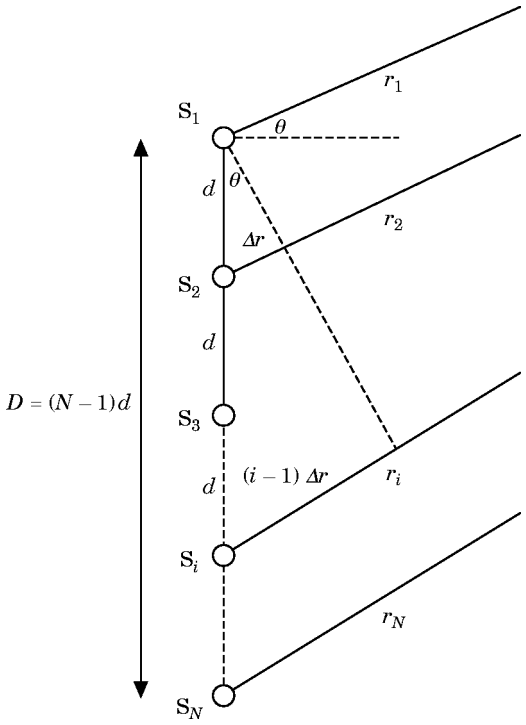

Figure A5. A linear array of N discrete sources.

or

$$P(r_o) = A(r)\,\mathrm{e}^{-\mathrm{j}kr_o} \sum_{n=0}^{n=N-1} (\mathrm{e}^{-\mathrm{j}k\Delta r})^n. \tag{A34}$$

Since for the sum

$$S_N = \sum_{i=0}^{N-1} (\mathrm{e}^{-\mathrm{j}\alpha})^i = 1 + \mathrm{e}^{-\mathrm{j}\alpha} + \mathrm{e}^{-\mathrm{j}2\alpha} + \mathrm{e}^{-\mathrm{j}3\alpha} + \cdots + \mathrm{e}^{-\mathrm{j}(N-1)\alpha} \tag{A35a}$$

the form:

$$S_N - \mathrm{e}^{-\mathrm{j}\alpha} S_N = 1 - \mathrm{e}^{-\mathrm{j}N\alpha}, \qquad \text{i.e.} \qquad S_N = (1 - \mathrm{e}^{-\mathrm{j}N\alpha})/(1 - \mathrm{e}^{-\mathrm{j}\alpha}), \tag{A35b}$$

generally applies, for the sum in expression (A34) one has

$$\sum_{n=0}^{n=N-1} (\mathrm{e}^{-\mathrm{j}k\Delta r})^n = \frac{1 - \mathrm{e}^{-\mathrm{j}k\Delta rN}}{1 - \mathrm{e}^{-\mathrm{j}k\Delta r}} = \frac{\mathrm{e}^{\mathrm{j}(k/2)\Delta r} - \mathrm{e}^{-\mathrm{j}[(k/2) - Nk]\Delta r}}{\mathrm{e}^{\mathrm{j}(k/2)\Delta r} - \mathrm{e}^{-\mathrm{j}(k/2)\Delta r}}$$

$$= \mathrm{e}^{-\mathrm{j}(k/2)(N-1)\Delta r}\left(\frac{\mathrm{e}^{\mathrm{j}(k/2)\Delta rN} - \mathrm{e}^{-\mathrm{j}(k/2)\Delta rN}}{\mathrm{e}^{\mathrm{j}(k/2)\Delta r} - \mathrm{e}^{-\mathrm{j}(k/2)\Delta r}}\right), \tag{A35c}$$

by using the identity $\sin x = (\mathrm{e}^{\mathrm{j}x} - \mathrm{e}^{-\mathrm{j}x})/2\mathrm{j}$, the expression for pressure $P(r)$ finally becomes

$$P(r_o) = A(r)\,\mathrm{e}^{-\mathrm{j}kr_o}\,\mathrm{e}^{-\mathrm{j}k(N-1)\Delta r/2}\chi_d. \tag{A36}$$

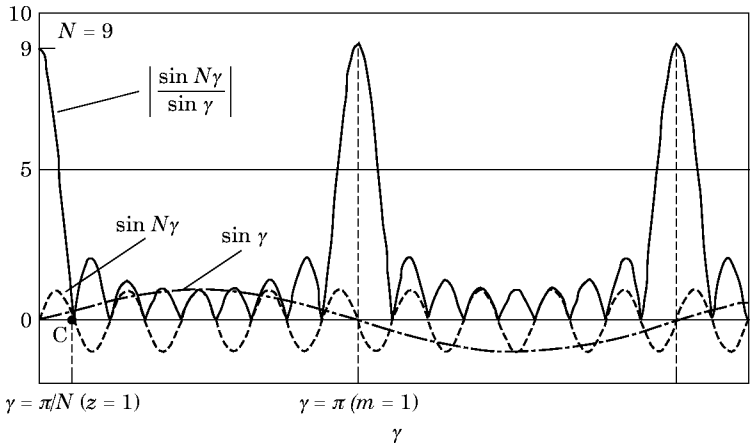

Figure A6. The discrete interference function $|\chi_d|$.

The exponential terms are phase angles and the discrete interference function χ_d is given by

$$\chi_d = (\sin N\gamma)/\sin\gamma, \tag{A37}$$

where

$$\gamma = k\Delta r/2 = (kd\sin\theta)/2 = (\pi d\sin\theta)/\lambda. \tag{A38}$$

The function $|\chi_d|$ is plotted in Figure A6 for the case $N = 9$ point sources. This function has two types of maxima, as follows.

(a) Major maxima occur when

$$\gamma = m\pi, \qquad m = 0, 1, 2, \ldots. \tag{A39}$$

For $m = 0$,

$$\chi_d = \lim_{\gamma\to 0}(\sin N\gamma)/(\sin\gamma) = N. \tag{A40}$$

For $m = 1$,

$$\gamma = \pi = (\pi d\sin\theta)/\lambda, \qquad \theta_{m1} = \sin^{-1}(\lambda/d). \tag{A41}$$

For good discrete representation (discreteness) $\theta_{m1} \geqslant 90^\circ$, giving $d \leqslant \lambda$, or for a more conservative definition, using $\gamma = \pi/2$ ($\sin\gamma = 1$) gives $d \leqslant \lambda/2$.

(b) Minor maxima occur when

$$N\gamma = (2n+1)\pi/2, \qquad n = 0, 1, 2, \ldots, N-2. \tag{A42}$$

For $n = 1$,

$$\gamma = 3\pi/2N = (\pi d\sin\theta_{n1})/\lambda, \qquad \theta_{n1} = \sin^{-1}(3\lambda/2Nd). \tag{A43}$$

Zeros of the same function are defined by

$$N\gamma = z\pi, \qquad z = 1, 2, 3, \ldots, N-1. \tag{A44}$$

For $z = 1$,

$$\gamma = \pi/N = (\pi d\sin\theta_{z1})/\lambda, \qquad \theta_{z1} = \sin^{-1}(\lambda/Nd), \tag{A45}$$

where the separation distance between a line of N sources of overall length D is

$$d = D/(N-1). \tag{A46}$$

The condition for source non-compactness, for $\theta \leqslant 90^\circ$, becomes

$$\gamma = [(\pi/\lambda)d \sin\theta]_{\theta \leqslant \pi/2} = \pi/N, \tag{A47}$$

giving

$$d \geqslant \lambda/N \qquad \text{or} \qquad D \geqslant [(N-1)/N]\lambda. \tag{A48}$$

For large N, conditions (A21) and (A48) become identical.

Thus the first zero determines the source non-compactness, and the second major maximum determines whether the source has good discrete representation.

It can be seen from Figure A6 that the number of zeros and minor maxima between two major maxima are given, respectively, by

$$N_z = N-1, \qquad N_n = N-2. \tag{A49}$$

In the case of multi-dimensional discrete sources as with continuous sources, multiple functions of the type χ_d must be included in expression (A36) for each dimension. The interference between point acoustic sources is equivalent to the effect of a diffraction grating in optics and X-ray diffraction in electromagnetics. For further information on optical and electromagnetic interference see, for example, references [5–7].